Inhibited KdpFABC resides in an E1 off-cycle state

Jakob M. Silberberg*[1], Charlott Stock*[1,2], Lisa Hielkema*[3], Robin A. Corey[4], Jan Rheinberger[3], Dorith Wunnicke[1], Victor R. A. Dubach[3], Phillip J. Stansfeld[5], Inga Hänelt[1‡], Cristina Paulino[3‡]

*Shared equal contributions
‡ Corresponding author
[1]Institute of Biochemistry, Biocenter, Goethe University Frankfurt, Max-von-Laue-Straße 9, 60438, Frankfurt/Main, Germany
[2]Current address: DANDRITE, Nordic EMBL Partnership for Molecular Medicine, Department of Molecular Biology and Genetics, Aarhus University, Universitetsbyen 81, DK-8000 Aarhus C, Denmark
[3]Department of Structural Biology, Groningen Biomolecular Sciences and Biotechnology Institute, University of Groningen, Nijenborgh 7, 9747 AG, Groningen, The Netherlands
[4]Department of Biochemistry, University of Oxford, South Parks Road, Oxford, OX1 3QU, UK
[5]School of Life Sciences & Department of Chemistry, University of Warwick, Coventry, CV4 7AL, UK

Abstract

KdpFABC is a high-affinity prokaryotic K^+ uptake system that forms a functional chimera between a channel-like subunit (KdpA) and a P-type ATPase (KdpB). At high K^+ levels, KdpFABC needs to be inhibited to prevent excessive K^+ accumulation to the point of toxicity. This is achieved by a phosphorylation of the serine residue in the $TGES_{162}$ motif in the A domain of the pump subunit KdpB ($KdpB_{S162\text{-}P}$). Here, we explore the structural basis of inhibition by $KdpB_{S162}$ phosphorylation by determining the conformational landscape of KdpFABC under inhibiting and non-inhibiting conditions. Under turnover conditions, we identified a new inhibited KdpFABC conformation that we termed E1-P tight, which is not part of the canonical Post-Albers transport cycle of P-type ATPases. It likely represents the biochemically described stalled E1-P state adopted by KdpFABC upon $KdpB_{S162}$ phosphorylation. The E1-P tight state exhibits a compact fold of the three cytoplasmic domains and is likely adopted when the transition from high-energy E1-P states to E2-P states is unsuccessful. This study represents a structural characterization of a biologically relevant off-cycle state in the P-type ATPase family and supports the emerging discussion of P-type ATPase regulation by such conformations.

Introduction

A steady intracellular K^+ concentration is vital for bacterial cells. Various export and uptake systems jointly regulate bacterial K^+ homeostasis when facing rapid changes in the environment (Diskowski et al., 2015; Stautz et al., 2021). KdpFABC is a primary active K^+ uptake system, which is produced when the extracellular K^+ supply becomes too limited for uptake by less affine translocation systems like KtrAB, TrkAH or Kup. Due to its high affinity for K^+ (K_M = 2 µM) and its active transport, KdpFABC can pump K^+ into the cell even at steep outward-directed gradients of up to 10^4, thereby guaranteeing cell survival (Altendorf et al., 1998; Epstein et al., 1993; Rhoads and Epstein, 1977).

The heterotetrametric KdpFABC complex comprises four subunits, namely the channel-like KdpA, a member of the superfamily of K^+ transporters (SKT) (Durell et al., 2000), the P-type ATPase KdpB (Hesse et al., 1984), the lipid-like stabilizer KdpF (Gaßel et al., 1999), and KdpC, whose function is still unknown. KdpB consists of a transmembrane domain (TMD) and the characteristic cytoplasmic nucleotide binding (N), phosphorylation (P) and actuator (A) domains. Analogous to all P-type ATPases, KdpB follows a Post-Albers reaction scheme, switching between E1 and E2 states that provide alternating access to the substrate binding site during turnover (Albers, 1967; Huang et al., 2017; Post et al., 1972; Silberberg et al., 2021; Stock et al., 2018; Sweet et al., 2021). Whilst in its outward-open E1 conformation, KdpFABC binds ATP in the N domain and takes up K^+ ions via the selectivity filter in KdpA, which progress into the intersubunit tunnel connecting KdpA and KdpB. Binding of ATP causes rearrangements of the cytoplasmic domains that result in nucleotide coordination between the N and P domains in the E1·ATP conformation. The γ-phosphate of ATP is coordinated in close proximity to the highly conserved $KdpB_{D307}$ of the P domain (all residue numbers refer to *Escherichia coli* KdpFABC). Upon binding of K^+ to the canonical binding site (CBS) of KdpB, $KdpB_{D307}$ cleaves off the ATP γ-phosphate *via* a nucleophilic attack, leading to the

autophosphorylation of KdpFABC and progression to the energetically unfavorable E1-P conformation. ATP cleavage releases the N domain from the P domain, allowing relaxing rearrangements of the cytoplasmic domains that convert KdpFABC to the inward-open E2-P state, in which K^+ is released from the CBS to the cytoplasm due to conformational changes in KdpB's TMD. Finally, $KdpB_{D307}$ is dephosphorylated by a water molecule coordinated by $KdpB_{E161}$ of the $TGES_{162}$ loop in the A domain, recycling KdpFABC via the non-phosphorylated E2 state back to its E1 ground state (Huang et al., 2017; Pedersen et al., 2019; Stock et al., 2018; Sweet et al., 2021). Thus, the relative orientation of the three cytoplasmic domains to each other and their nucleotide state (nucleotide-free, nucleotide-bound, or phosphorylated) are crucial for the assignment of catalytic states (Bublitz et al., 2010; Dyla et al., 2020). Notably, while the general catalytic reaction and conformational arrangements of the N, P and A domains follow the conventional Post-Albers cycle observed for other P-type ATPases, the alternating access of the substrate binding site in the KdpFABC complex is inverted to accommodate KdpFABC's unique inter-subunit transport mechanism involving KdpA and KdpB (Damnjanovic et al., 2013; Silberberg et al., 2021; Stock et al., 2018).

Being a highly efficient emergency K^+ uptake system, KdpFABC needs to be tightly regulated in response to changing K^+ conditions, as both too low and too high potassium concentrations would be toxic (Roe et al., 2000; Stautz et al., 2021). At low K^+ conditions, transcription of the *kdpFABC* operon is activated by the K^+-sensing KdpD/KdpE two-component system (Polarek et al., 1992). Further, post-translational stimulation is conferred by cardiolipin, whose concentration increases as a medium-term response to K^+ limitation (Schniederberend et al., 2010; Silberberg et al., 2021). Once K^+ stress has abated ($[K^+_{external}] > 2$ mM), the membrane-embedded KdpFABC is rapidly inhibited to prevent excessive uptake of K^+ (Roe et al., 2000). This is achieved by a post-translational phosphorylation of $KdpB_{S162}$ (yielding $KdpFAB_{S162\text{-}P}C$), which is part of the highly conserved $TGES_{162}$ motif of the A domain (Huang

et al., 2017; Sweet et al., 2020). In the crystal structure of KdpFABC [5MRW], phosphorylated $KdpB_{S162}$ forms salt bridges with $KdpB_{K357}$ and $KdpB_{R363}$ of the N domain and adopts an unusual E1 conformation. It was suggested that the salt bridge formation inhibits KdpFABC by locking the complex in this conformation (Huang et al., 2017). However, the salt bridges were shown to be non-essential to the inhibition mechanism, leaving the role of this conformation unclear (Stock et al., 2018; Sweet et al., 2020). Recent functional studies showed that $KdpB_{S162}$ phosphorylation stalls the complex in an intermediate E1-P state, preventing the transition to the inward-open E2-P conformation (Sweet et al., 2020).

Here, we set out to address the structural basis for KdpFABC inhibition by $KdpB_{S162}$ phosphorylation. The conformational landscape of KdpFABC was probed under different conditions by cryo-EM, yielding 10 structures representative of 6 distinct states that describe the full conformational spectrum of the KdpFABC catalytic cycle and resolve the effect of the inhibitory phosphorylation on the conformational plasticity of the complex. Distinct conformational states were further characterized by pulsed EPR measurements and MD simulations to decipher how $KdpB_{S162}$ phosphorylation leads to the inhibition of the complex in the high-energy E1-P intermediate.

Results

Previous structural studies of KdpFABC were exclusively conducted in the presence of conformation-specific inhibitors (Huang et al., 2017; Silberberg et al., 2021; Stock et al., 2018; Sweet et al., 2021). To describe the structural effects of KdpFABC inhibition by $KdpB_{S162}$ phosphorylation, we prepared cryo-EM samples of KdpFABC variants under conditions aimed at covering the conformational landscape of both the non-phosphorylated, active and the phosphorylated, inhibited complex (Table 1; Table 1 – Table Supplement 1). For this, all KdpFABC variants were produced in *Escherichia coli* at high K^+ concentration, which is

known to lead to the inhibitory $KdpB_{S162}$ phosphorylation (Sweet et al., 2020). Then, $KdpFAB_{S162A}C$, a non-phosphorylatable $KdpB_{S162}$ variant, and wild type KdpFABC ($KdpFAB_{S162\text{-}P}C$) were analyzed under turnover conditions, i.e., in the presence of saturating KCl and ATP concentrations, to gain insights into the dynamic conformational landscape adopted by the complex. To supplement these samples, inhibited WT $KdpFAB_{S162\text{-}P}C$ was prepared in the presence of orthovanadate, known to normally arrest P-type ATPases in an E2 state. Further, the catalytically inactive variant $KdpFAB_{S162\text{-}P/D307N}C$ was prepared under nucleotide-free conditions to investigate E1 apo states. In sum, the 10 maps obtained from the four samples cover the entire KdpFABC conformational cycle. All structures exhibit the same intersubunit tunnel described previously, which varies in length depending on the state, and is filled with densities assigned as K^+ ions (Silberberg et al., 2021; Stock et al., 2018). Between structures, the ion densities vary slightly in number and position (Table 1 – Figure Supplement 1).

Table 1: Conformational landscape of KdpFABC resolved by cryo-EM. Four samples were prepared for cryo-EM analysis. Structural models were built for all maps with a resolution of 4 Å or below.

Protein sample	Condition	State/Resolution						
		E1 apo open		E1 apo tight	$E1{\cdot}ATP_{early}$	E1-P·ADP	E1-P tight	E2-P
		Sub-state 1	Sub-state 2					
$KdpFAB_{S162\text{-}P}C$	50 mM KCl 2 mM ATP ("turnover")				3.5 Å	3.1 Å	3.4 Å	
	1 mM KCl 2 mM VO_4^{3-}						3.3 Å	7.4 Å
$KdpFAB_{S162\text{-}P/D307N}C$	50 mM KCl	3.5 Å	3.7 Å	3.4 Å				
$KdpFAB_{S162A}C$	50 mM KCl 2 mM ATP ("turnover")					3.7 Å		4.0 Å

Non-inhibited KdpFABC transitions through the Post-Albers cycle under turnover conditions

Previous functional and structural studies have shown that non-phosphorylatable $KdpFAB_{S162A}C$ can adopt major states of the Post-Albers cycle (Sweet et al., 2021, 2020). However, the different conformations were captured with the help of various state-specific

inhibitors, limiting our understanding of KdpFABC's full conformational landscape. To determine the predominant states under turnover conditions, non-phosphorylatable KdpFAB$_{S162A}$C was incubated with 2 mM ATP and 50 mM KCl for 5 minutes at RT immediately before plunge freezing and analyzed by cryo-EM. From this dataset, we obtained 'only' two structures of KdpFABC (Figure 1; Table 1; Figure 1 – Figure Supplement 1–2; Table 1 – Table Supplement 1).

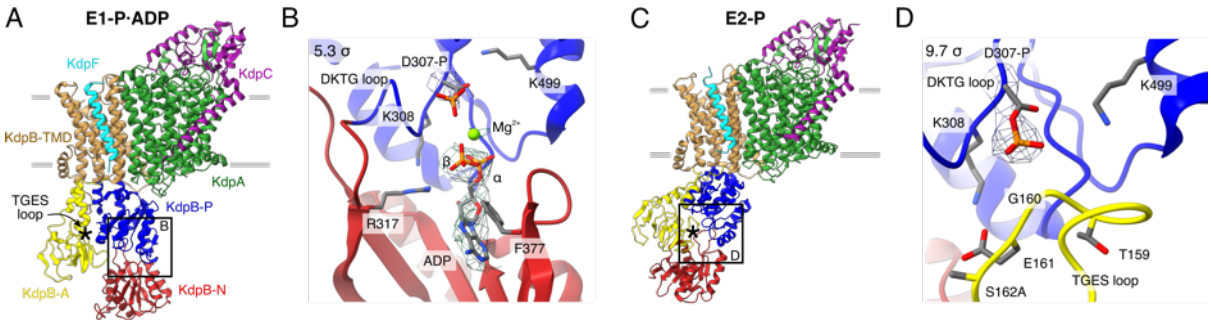

Figure 1: Structures of KdpFAB$_{S162A}$C obtained at turnover conditions. Color code throughout the manuscript, unless stated otherwise, is as follows: KdpF in cyan, KdpA in green, KdpC in purple, KdpB TMD in sand with P domain in blue, N domain in red and A domain in yellow and position of the TGES$_{162}$ loop denoted by an asterisk. **A** E1-P·ADP structure, with its nucleotide binding site (**B**), showing the bound ADP with Mg^{2+}. **C** E2-P structure, with its nucleotide binding site (**D**), showing the catalytically phosphorylated KdpB$_{D307}$ (P domain), and the TGES$_{162}$ loop (A domain) in close proximity. Densities are shown at the indicated σ level.

The first structure, resolved globally at 3.7 Å and derived from ~35% of the initial particle set, shows an E1 state. The overall orientation of the cytosolic domains is reminiscent of our previously published E1·ATP structure [7NNL] (Figure 1A; Figure 1 – Figure Supplement 2E) (Silberberg et al., 2021). However, closer inspection of the N domain reveals no density around the expected γ-phosphate of ATP, whereas additional density is observed near KdpB$_{D307}$. We interpret that ADP, instead of ATP, is bound and the catalytic aspartate KdpB$_{D307}$ has been phosphorylated (Figure 1B). An additional density observed near the phosphorylated KdpB$_{D307}$ coincides with an Mg^{2+} ion in the E1-P·ADP SERCA structure [1T5T] (Sørensen et al., 2004), and has thus likewise been assigned as a coordinating Mg^{2+} ion (Figure 1B). Altogether, this conformation represents an E1-P·ADP state, following ATP hydrolysis but preceding the

release of ADP. The second structure obtained from the KdpFAB$_{S162A}$C sample under turnover conditions was resolved globally at 4.0 Å from ~28% of the initial particle set. In this structure, KdpB$_{D307}$ is phosphorylated and the TGES$_{162}$ loop is in close proximity, which is the hallmark of a E2-P conformation (Figure 1C,D). This resembles the previously published E2-P structure [7BH2], which was stabilized by the phosphate analogue BeF_3^- (Figure 1 – Figure Supplement 2J) (Sweet et al., 2021). In comparison to the E1-P·ADP state, the A domain in the E2-P state has undergone a tilt of 60° and a rotation of 64° around the P domain, positioning the TGES$_{162}$ loop to dephosphorylate KdpB$_{D307}$ in the P domain, while the P domain is also tilted by 40° (Figure 1 – Figure Supplement 3).

The E1-P·ADP and E2-P structures obtained for KdpFAB$_{S162A}$C confirm that, in the absence of the inhibitory KdpB$_{S162}$ phosphorylation, KdpFABC progresses through the entire Post-Albers cycle under turnover conditions, with the ADP release in the E1 conformation and the dephosphorylation of KdpB$_{D307}$ in the E2 conformation likely being the rate-limiting steps that lead to an accumulation of the observed states.

Inhibited E1-P KdpFABC adopts an off-cycle conformation

To study the structural implications of KdpFABC inhibition by KdpB$_{S162}$ phosphorylation, we next analyzed the conformational landscape of WT KdpFAB$_{S162\text{-}P}$C under turnover conditions. To our surprise, the dataset disclosed a higher degree of conformational variability than KdpFAB$_{S162A}$C, yielding three distinct cryo-EM structures (Figure 2; Table 1; Figure 2 – Figure Supplement 1–2; Table 1 – Table Supplement 1). The obtained structures show significant deviations in the cytoplasmic region of KdpB, indicative of different positions in the conformational cycle.

The first KdpFAB$_{S162\text{-}P}$C turnover structure, resolved at an overall resolution of 3.5 Å and derived from ~9% of the initial particle set, resembles the E1·ATP structure [7NNL]

(Silberberg et al., 2021) (Figure 2A; Figure 2 – Figure Supplement 2E). However, a closer analysis of the cytosolic domains and the bound nucleotide reveals significant differences. While ATP is coordinated in a similar fashion as previously observed (Silberberg et al., 2021; Sweet et al., 2021), the N domain is slightly displaced relative to the P domain, providing more access to the nucleotide binding site (Figure 2A,B; Figure 2 – Figure Supplement 2E). We interpret this structure as an E1·ATP conformation at an early stage of nucleotide binding and refer to it as E1·ATP$_{early}$. By contrast, inhibitors such as AMPPCP likely stabilize the latest possible and otherwise transient E1·ATP state right before hydrolysis, explaining the discrepancy between the AMPPCP-stabilized [7NNL] and the E1·ATP state obtained here under turnover conditions. The second KdpFAB$_{S162\text{-}P}$C turnover structure, resolved at an overall resolution of 3.1 Å and representing ~31% of the initial particle set, is virtually identical to the above-described E1-P·ADP conformation of KdpFAB$_{S162A}$C (Figure 2C,D; Figure 2 – Figure Supplement 2J).

While the first two structures represent known states of the catalytic cycle, the third KdpFAB$_{S162\text{-}P}$C structure obtained under turnover conditions shows an unusual compact conformation of the cytosolic domains not yet observed in the Post-Albers cycle of other P-type ATPases (Figure 2E,F). The structure was resolved at an overall resolution of 3.4 Å and derived from ~14% of the initial particle set. Strikingly, the N domain is closely associated with the A domain, thereby disrupting the nucleotide binding site between the N and P domains (Figure 2E,F; Figure 2 – Figure Supplement 3). Closer inspection of the nucleotide binding site shows that the catalytic aspartate KdpB$_{D307}$ is phosphorylated, but not located in proximity to the TGES$_{162}$ loop of the A domain (Figure 2F). This indicates that the conformation is adopted after the canonical E1-P state, which in a normal non-inhibited catalytic cycle would transition into an E2-P state. Due to its compact organization, we termed this conformation E1-P tight.

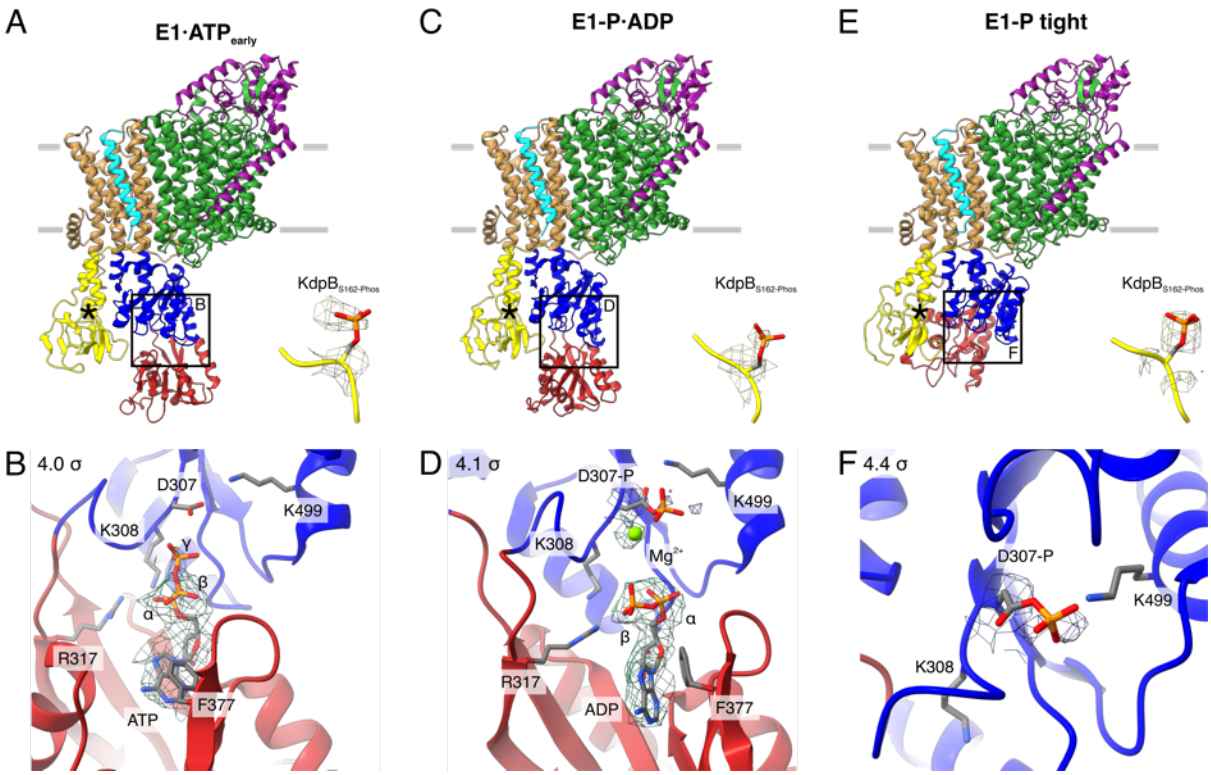

Figure 2: Structures of WT KdpFAB$_{S162\text{-}P}$C obtained at turnover conditions. A E1·ATP$_{early}$ structure with the corresponding density of KdpB$_{S162}$ phosphorylation and **(B)** its nucleotide binding site, showing the bound ATP. **C** E1-P·ADP structure with the corresponding density of KdpB$_{S162}$ phosphorylation and **(D)** its nucleotide binding site, showing the bound ADP with Mg^{2+}. Densities are shown for KdpB$_{D307\text{-}P}$, Mg^{2+}, and ADP. **E** E1-P tight structure with the corresponding density for KdpB$_{S162}$ phosphorylation and **(F)** its nucleotide binding site. Densities are shown at the indicated σ level.

Previous biochemical studies have shown that KdpB$_{S162}$ phosphorylation inhibits KdpFABC by preventing the transition to an E2 state and stalling it in an E1-P state (Sweet et al., 2020). In line with these observations, we could not identify any conformation following E1-P in the Post-Albers cycle for KdpFAB$_{S162\text{-}P}$C, despite the turnover conditions used. Based on this, we hypothesized that the novel E1-P tight state observed represents a non-Post-Albers conformation that is adopted because KdpFAB$_{S162\text{-}P}$C cannot proceed to the E2-P state. To further put this to test, we analyzed the conformations adopted by WT KdpFAB$_{S162\text{-}P}$C in the presence of the phosphate mimic orthovanadate, which has been shown to trap P-type ATPases in an E2-P conformation and, of all E2 state inhibitors, best mimics the charge distribution of a bound phosphate (Table 1; Figure 2 – Figure Supplement 4–5; Table 1 – Table Supplement 1) (Clausen et al., 2016; Pedersen et al., 2019). Interestingly, KdpFAB$_{S162\text{-}P}$C incubated with

2 mM orthovanadate prior to cryo-EM sample preparation did not conform to this behavior. Instead, the major fraction of this sample (~62% of the initial particle set) resulted in an E1-P tight conformation, resolved at 3.3 Å, which is virtually identical to the E1-P tight conformation obtained under turnover conditions (Figure 2 – Figure Supplement 3H). The position of the orthovanadate coincides with that adopted by the phosphorylated $KdpB_{D307}$, verifying the assignment of this state as a phosphorylated E1-P intermediate (Figure 2 – Figure Supplement 5). Only a minor fraction of the orthovanadate-stabilized sample (~11% of the initial particle set) adopts an E2-P conformation. Despite the rather poor resolution of 7.4 Å, the conformational state could be confirmed by comparison of the cryo-EM map with the previously published E2-P structure [7BH2] (Figure 2 – Figure Supplement 4I) (Sweet et al., 2021). The minor fraction found in an E2 state likely represents the residual KdpFABC in the sample lacking $KdpB_{S162}$ phosphorylation, as it is in good agreement with the residual ATPase activity level (Sweet et al., 2020). The fact that, in the presence of orthovanadate, $KdpFAB_{S162\text{-}P}C$ adopts the E1-P tight state instead of an E2-P conformation strongly supports the idea that the inhibited complex cannot transition into an E2 state but instead adopts an off-cycle E1-P state after ADP dissociation.

A tight conformation is also formed in the absence of nucleotide

Interestingly, the close association of the N domain with the A domain in the E1-P tight conformation also shows some similarities to the E1 crystal structure of KdpFABC [5MRW], the first structure of KdpFABC ever solved (Huang et al., 2017). Unlike our E1-P tight state, the crystal structure is nucleotide-free and does not contain a phosphorylated $KdpB_{D307}$, raising the question how it fits in the conformational landscape of KdpFABC. To further investigate the role of the tight conformation in the conformational cycle of KdpFABC, we prepared a cryo-EM sample of $KdpFAB_{S162\text{-}P/D307N}C$ under nucleotide-free conditions. This mutant is

catalytically inactive and thus restricted to E1 states preceding ATP hydrolysis. In total, we were able to obtain three distinct structures from this preparation, which we assigned to two states relevant to the transport cycle (Figure 3, Table 1; Figure 3 – Figure Supplement 1–2; Table 1 – Table Supplement 1).

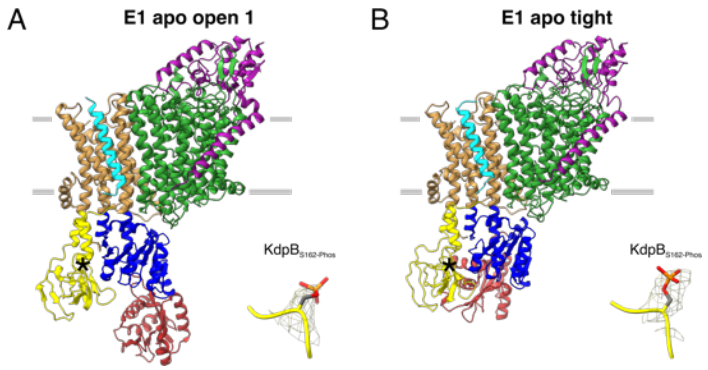

Figure 3: E1 apo structures of KdpFAB$_{S162\text{-}P/D307N}$C obtained at nucleotide-free conditions. A E1 apo open substate 1 structure with the corresponding density of KdpB$_{S162}$ phosphorylation. The E1 apo open substate 2 differs by a slightly displaced orientation of the N domain (see also Figure 3 – Figure Supplement 1,2). **B** E1 apo tight structure with the corresponding density of KdpB$_{S162}$ phosphorylation.

The first state, composed of 26% of the initial particle set from the nucleotide-free sample, corresponds to the canonical Post-Albers E1 state that precedes ATP binding and resembles the E1 apo state [7BH1] reported previously (Sweet et al., 2021) (Figure 3A; Figure 3 – Figure Supplement 2E). We have termed this conformation the E1 apo open state, as the N and P domains are far apart to provide access to the nucleotide binding site. The cytosolic domains of KdpB reveal a high conformational heterogeneity, evidenced by their lower local resolution (Figure 3 – Figure Supplement 2B,G). Focused 3D classification allowed the distinction of two substates, resolved globally at 3.5 Å and 3.7 Å, differing in the relative position of the N to the P domain (Figure 3 – Figure Supplement 2J). The high degree of flexibility of the N domain in this open conformation likely facilitates nucleotide binding at the start of the Post-Albers cycle. The second state, featuring one structure resolved globally at 3.4 Å and represented by 19% of the initial particle set, shows a compact conformation of the cytosolic domains with the N and

A domains in close contact, providing no space for a nucleotide to bind (Figure 3C). This state is similar, but not identical to the one observed in the E1-P tight state and [5MRW], and we have termed it the E1 apo tight state (Figure 3 – Figure Supplement 2O). The presence of a similar tight conformation in both the E1-P and the E1 apo states of $KdpB_{S162\text{-}P}$, shows that, while the inhibitory $KdpB_{S162}$ phosphorylation appears to be a prerequisite, the observed close association of the N and A domains can occur before or after the binding and hydrolysis of ATP.

The tight state interaction between the N and A domains is itself not the cause of inhibition

Structures with a tight arrangement of the A and N domains were only obtained in cryo-EM samples featuring $KdpB_{S162\text{-}P}$. To evaluate the dependency of a tight state formation on $KdpB_{S162}$ phosphorylation, we assessed the full conformational flexibility of the N domain using pulsed EPR spectroscopy. Distances between the N and P domains were measured with the labeled residues $KdpB_{A407CR1}$ and $KdpB_{A494CR1}$ (Figure 4A,B; Figure 4 – Figure Supplement 1). Variants were produced at high K^+ concentrations to confer $KdpB_{S162}$ phosphorylation. EPR analysis of $KdpFAB_{S162\text{-}P/D307N}C$ in the absence of nucleotide resulted in distances that resemble the E1 apo tight and the E1 apo open conformations (Figure 4B). This corroborates the cryo-EM results that both tight and open states are adopted in the same sample at nucleotide-free conditions. In contrast, the non-phosphorylatable variant $KdpB_{S162A}$ resulted in a distance distribution showing a near total elimination of the E1 apo tight state. This strongly indicates that the tight state is stabilized by $KdpB_{S162}$ phosphorylation, although it still exists to a small extent even in the absence of the inhibitory phosphorylation.

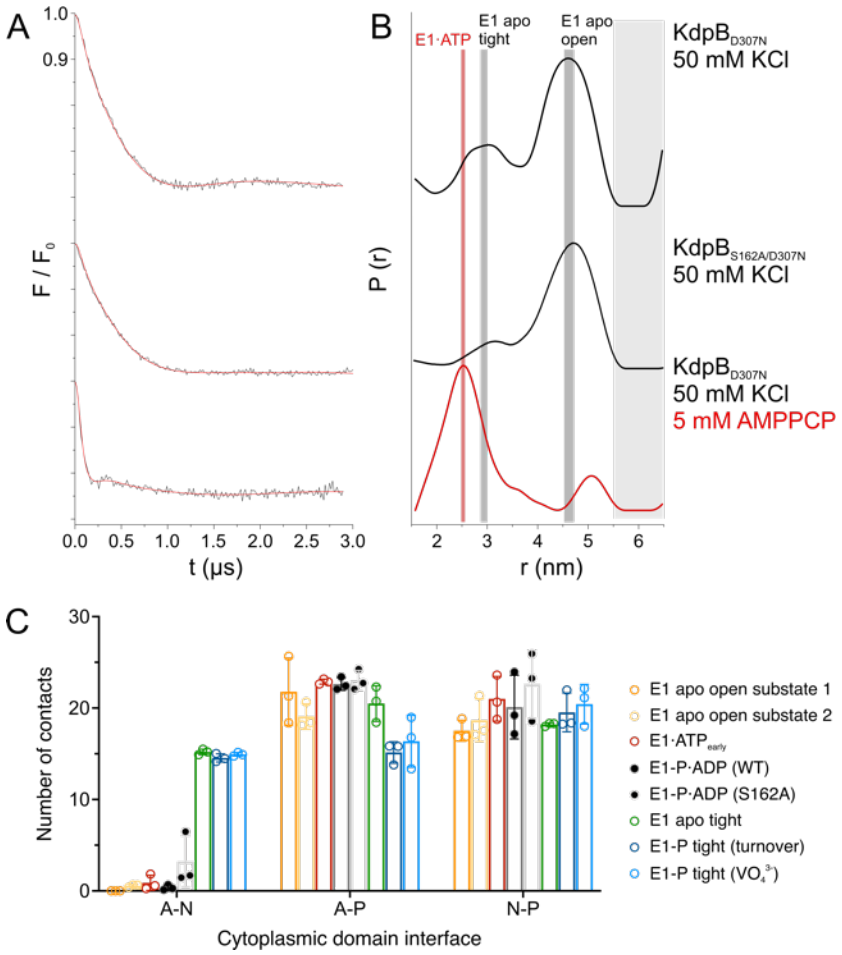

Figure 4: KdpB$_{S162-P}$ increases interdomain contacts in E1 tight states. A Background-corrected dipolar evolution function F(t) with applied fit (red lines) of DEER measurements. **B** Area-normalized interspin distance distribution P(r) obtained by Tikhonov regularization. Two KdpFABC variants were prepared with 50 mM KCl and in the presence (red curve) or absence (black curves) of 5 mM AMPPCP. KdpFAB$_{D307N}$C and KdpFAB$_{S162A/D307N}$C without AMPPCP show two conformations, with N-P domain distances of 3 nm and 4.5 nm corresponding to the E1 apo tight and E1 apo open states (dominant state), respectively, as indicated by dark grey background shading. The removal of the inhibitory phosphorylation site in KdpFAB$_{S162A/D307N}$C showed a significant decrease of the distance corresponding to the E1 apo tight state (3 nm) compared to KdpFAB$_{D307N}$C. Addition of AMPPCP to KdpFAB$_{D307N}$C resulted in a single stabilized distance of 2.5 nm, representing the E1·ATP conformation as indicated by red background shading. Light grey shaded areas starting at 5.5 nm indicate unreliable distances. **C** Contact analysis between the N, P and A domains for all E1 structures obtained in this study. Average of the number of contacts (>90% contact) between the different domains over 3 x 50 ns MD simulations (see also Figure 4 – Figure Supplement 2 for details of identified high-contact interactions). Interactions between A and P or N and P domains remain consistent across all states, while interactions between A and N domains are increased only in E1 tight conformations.

To inspect what makes the off-cycle tight conformations energetically preferable, we quantified the cytosolic domain interactions of all E1 states obtained in this study using contact analysis by molecular dynamics (MD) simulation (Figure 4C; Figure 4 – Figure Supplement 2). While no large differences are observed for the contacts between A and P or N and P domains, the off-cycle E1 tight states (E1 apo tight, E1-P tight) are the only ones to show a higher number

of interactions between the A and N domains. In fact, they share a nearly identical number of contacts, indicating that the A and N domains move in a concerted manner, similar to previous observations by MD simulations (Dubey et al., 2021). The most evident interaction seen in all three tight states is formed by the salt bridges between the phosphate of $KdpB_{S162\text{-}P}$ in the A domain and $KdpB_{K357/R363}$ in the N domain, which were first described in [5MRW] (Huang et al., 2017). However, functional studies have shown that these salt bridges are not essential for the inhibition (Sweet et al., 2020), and neither are they sufficient to fully arrest a tight state, as shown here. In agreement to this, EPR measurements with $KdpFAB_{S162\text{-}P/D307N}C$ in the presence of the ATP analogue AMPPCP result in a distance distribution that shows a single and well-defined distance, which corresponds to the E1·ATP state. Hence, the salt bridges and the enhanced interaction platform between the A and N domain seen in the tight states likely have a stabilizing role, but can be easily broken and are themselves not the main cause of inhibition.

E1-P tight is the consequence of an impaired E1-P/E2-P transition

As the compact arrangement found in the E1 tight states itself is not the determining factor of inhibition, the question remains how K^+ transport is blocked in $KdpFAB_{S162\text{-}P}C$ and what role the E1-P tight state plays. In a non-inhibited transport cycle, KdpFABC rapidly relaxes from the high-energy E1-P state into the E2-P conformation. To identify what structural determinants enable the arrest before this transition, we compared the E1-P tight structure with the other structures obtained in this study (Figure 5). The E1-P tight state features a tilt of the A domain by 26° in helix 4 ($KdpB_{198\text{-}208}$) that is not found in the other E1 states, including the E1 apo tight state (Figure 5B,C – arrow 1). This tilt is reminiscent of the movement the A domain undergoes during the E1-P/E2-P transition (60° tilt, Figure 1 – Figure Supplement 3), but not as far and does not feature the rotation around the P domain

(Figure 5 – Figure Supplement 1B,C). Moreover, the P domain does not show the tilt observed in the normal E1-P/E2-P transition. Notably, this is the movement that brings $KdpB_{D307\text{-}P}$ in close proximity of $KdpB_{S162}$ in the catalytic cycle (Figure 5 – Figure Supplement 2, Video 1). In an inhibited state, where both sidechains are phosphorylated, such a transition is most likely impaired due to the large charge repulsion. A comparison of the E1-P tight structure with the E1-P·ADP structure, its immediate precursor in the conformational cycle, moreover, reveals a number of significant rearrangements within the P domain (Figure 5B,C). First, Helix 6 ($KdpB_{538\text{-}545}$) is partially unwound and has moved away from helix 5 towards the A domain, alongside the tilting of helix 4 of the A domain (Figure 5B,C – arrow 2). Second, and of particular interest, are the additional local changes that occur in the immediate vicinity of the phosphorylated $KdpB_{D307}$. In the high-energy E1-P·ADP structure, the catalytic aspartyl phosphate, located in the D_{307}KTG signature motif, points towards the negatively charged $KdpB_{D518/D522}$. This repulsion might serve as a driving force for the system to relax into the E2 state in the catalytic cycle. By contrast, the D_{307}KTG loop is largely uncoiled in the E1-P tight state, with the phosphorylated $KdpB_{D307}$ pointing in the opposite direction, releasing this electrostatic strain (Figure 5C – arrow 4). This conformation is further stabilized by a salt bridge formed with $KdpB_{K499}$. The uncoiling in the E1-P tight conformation is likely mediated by the movement of the N domain towards the A domain, as the N domain is directly connected to the D_{307}KTG loop (Figure 5C – arrow 3). Altogether, we propose that, in presence of the inhibitory $KdpB_{S162\text{-}P}$, the high-energy E1-P·ADP state can no longer transition into an E2-P state after release of ADP and Mg^{2+}. As a consequence, the conformational changes observed in the E1-P tight state likely ease the electrostatic tensions of the phosphorylated P domain and stall the system in a ‘relaxed’ off-cycle state.

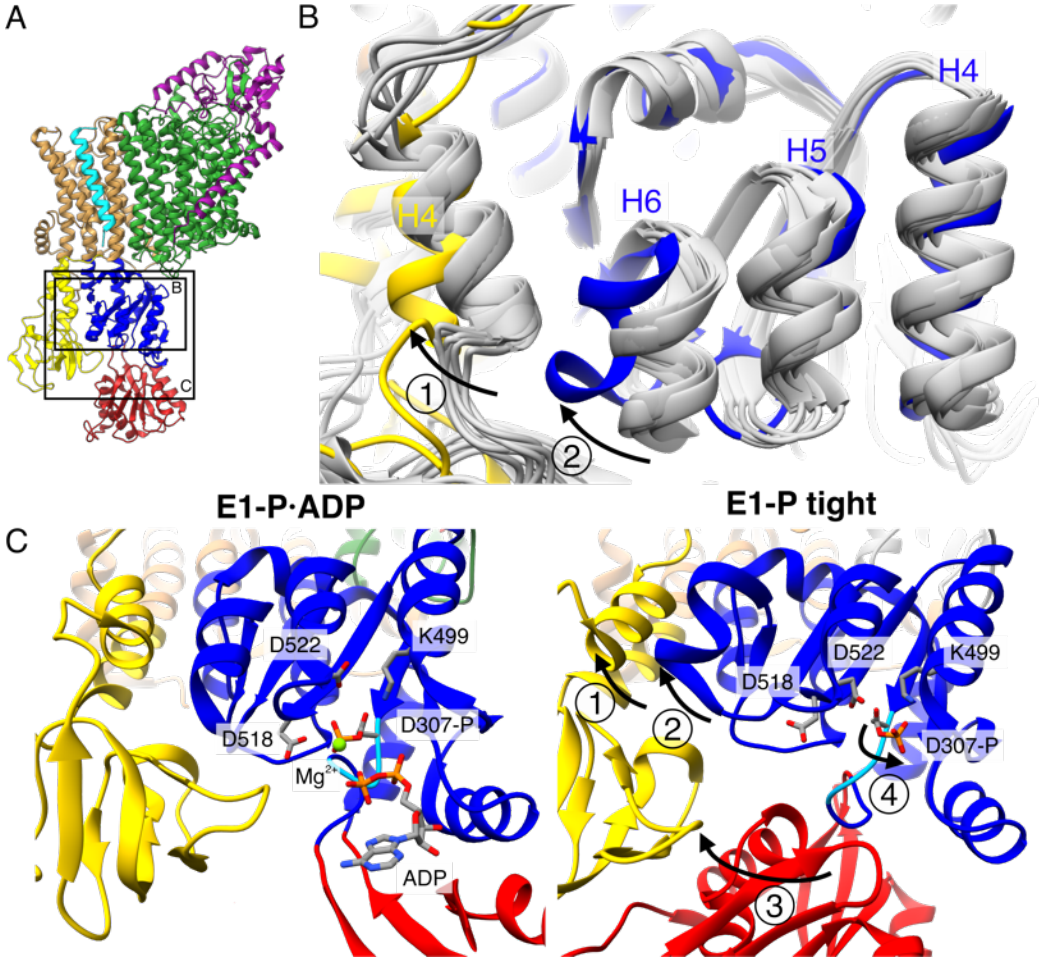

Figure 5: Structural rearrangements in the E1-P tight state facilitate KdpFAB$_{S162\text{-}P}$C stalling. A Structure of KdpFAB$_{S162\text{-}P}$C in the E1-P tight state obtained at turnover conditions. **B** Overlay of all E1 structures determined in this study (in gray) shows helix rearrangements particular to the E1-P tight state (in color). Arrow 1 indicates how the A domain helix 4 tilts away from the TMD by 26°; Arrow 2 indicates how P domain helix 6 moves along with A domain helix 4, slightly uncoiling and shifting away from the remaining P domain. **C** Vicinity of the catalytic aspartyl phosphate (KdpB$_{D307\text{-}P}$) in the KdpFAB$_{S162\text{-}P}$C E1-P·ADP and E1-P tight structures, showing rearrangements in the P domain to ease tensions of the E1-P state. In the high-energy E1-P·ADP state, KdpB$_{D307\text{-}P}$ shows strong electrostatic clashes with KdpB$_{D518/D522}$ (2.9 and 3.5 Å, respectively). These are alleviated by rearrangements in the E1-P tight state. Arrow 3 indicates the movement of the N domain towards the A domain in the tight conformation, which pulls on the D$_{307}$KTG loop (light blue) containing the aspartyl phosphate to uncoil and reorient it. Arrow 4 indicates how this rearrangement reorients the phosphorylated KdpB$_{D307\text{-}P}$ away from KdpB$_{D518/D522}$ (7.8 and 4.1 Å, respectively) to form a salt bridge with KdpB$_{K499}$ (3.9 Å).

Discussion

We set out to deepen our understanding of the structural basis of KdpFABC inhibition via KdpB$_{S162}$ phosphorylation by sampling the conformational landscape under various conditions by cryo-EM. The 10 cryo-EM maps of KdpFABC, which represent six distinct states, cover the full conformational landscape of KdpFABC and, most importantly, uncover a non-Post-Albers regulatory off-cycle state involved in KdpFABC inhibition (Figure 6).

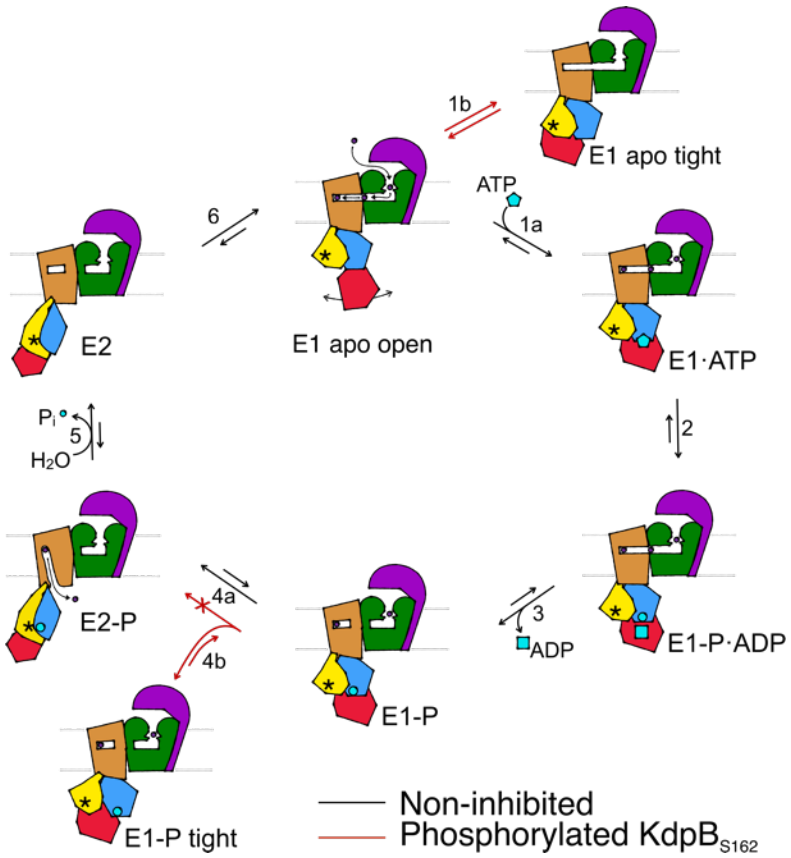

Figure 6: Proposed transport cycle of KdpFABC in the absence and presence of regulatory phosphorylation at $KdpB_{S162}$. Black arrows indicate the non-inhibited catalytic cycle, while red arrows denote the transitions taken when $KdpB_{S162}$ is phosphorylated, and the complex is inhibited. ATP shown as cyan pentagon; ADP as cyan rectangle; phosphorylated $KdpB_{D307}$ as cyan circle; K^+ ions in dark purple; the position of the $TGES_{162}$ loop in the A domain as an asterisk; KdpF is removed for simplicity.

The catalytic conformations identified here closely adhere to the classical Post-Albers cycle of KdpFABC (Video 1). In the outward-facing E1 apo open state, the nucleotide binding domain is widely accessible, and the N domain shows a high degree of flexibility, which likely enhances the efficiency of nucleotide binding from the environment. Once a nucleotide is bound, the N domain reorients towards the P domain for shared coordination of the nucleotide in the $E1{\cdot}ATP_{early}$ state (Figure 6, transition 1a). This conformation shows a slightly more open nucleotide-bound state than the previously reported AMPPCP-stabilized E1·ATP state, which likely can progress closer to ATP hydrolysis (Silberberg et al., 2021; Sweet et al., 2021). Subsequently, ATP cleavage leads to the phosphorylation of the catalytic $KdpB_{D307}$ in the P domain, forming the E1-P·ADP intermediate (Figure 6, transition 2), which could be

structurally isolated in this study under turnover conditions. The accumulation of the E1-P·ADP state in both turnover samples analyzed in this study suggests that ADP and Mg^{2+} release (Figure 6, transition 3) is the rate-limiting step of KdpFABC turnover. Following the catalytic cycle, the high-energy E1-P state progresses to the E2-P state, whereby large rearrangements bring the conserved $TGES_{162}$ loop in the A domain near the catalytic site of the P domain. This transition is accompanied by conformational changes in the TMD of KdpB, which switches the complex from an outward- to an inward-open state with respect to the CBS (Figure 6, transition 4a). K^+ is released to the cytosol and $KdpB_{D307\text{-}P}$ is dephosphorylated by the $TGES_{162}$ loop (Figure 6, transition 5). Subsequently, the complex cycles back to the E1 apo open state (Figure 6, transition 6).

Whereas the structures obtained for $KdpFAB_{S162\text{-}P}C$ in the E1 apo open, E1·ATP, E1-P·ADP and E2-P conformations align well with corresponding states in the Post-Albers cycle of other P-type ATPases, the nucleotide-free E1 apo tight and E1-P tight states do not. Their overall compact fold is facilitated by $KdpB_{S162\text{-}P}$, which increases the contacts of the N and A domains. While the compact fold itself is not the main cause of stalling KdpFABC, it might contribute to stabilizing the inhibited complex limiting the innate flexibility of the N domain. Thus, the E1 apo tight state likely has no major physiological relevance, as in presence of ATP, it would progress through the catalytic cycle up to the point of inhibition.

By contrast, we propose that the E1-P tight state is involved in stalling the KdpFABC complex. We suggest that this state represents the biochemically described E1-P inhibited state (Sweet et al., 2020), and is adopted after ADP release from the high-energy E1-P state, when KdpFABC attempts to relax into the E2-P state (Figure 6, transition 4b). This attempt would explain the partial tilt of the A domain in helix 4, observed only in the E1-P tight structure. As suggested before (Sweet et al., 2020), the full relaxation to the E2-P state is however hindered in the inhibited $KdpFAB_{S162\text{-}P}C$ by a repulsion between the catalytic phosphate in the P domain

426 ($KdpB_{D307\text{-}P}$) and the inhibitory phosphate in the A domain ($KdpB_{S162\text{-}P}$), which would come in
427 close proximity during the transition from E1-P to E2-P (Figure 6, transition 4a, Video 1). The
428 adopted stalled E1-P tight state is likely an energetically favored conformation between E1-P
429 and E2-P, easing the high-energy constraints around the phosphorylated $KdpB_{D307}$. In good
430 agreement with this hypothesis, $KdpFAB_{S162\text{-}P}C$ was stabilized in the E1-P tight conformation
431 even in the presence of the inhibitor orthovanadate, known to otherwise stabilize an E2-P state.
432 Notably, orthovanadate has the same charge distribution as the E1-P tight state with
433 phosphorylated $KdpB_{D307}$. By contrast, $KdpFAB_{S162\text{-}P}C$ in the presence of AlF_4^-, which has a
434 negative charge less, could previously be stabilized in an E2-P state (Stock et al., 2018), likely
435 because the electrostatic repulsion is lower, making the E1-P/E2-P transition more favorable.
436 For a long time, E1-P states of P-type ATPases have been biochemically characterized as high-
437 energy intermediates. However, the structural determinants for this energetic unfavorability
438 have yet to be described. The conformational changes we observe between the E1-P·ADP state
439 and the relaxed E1-P tight conformation offer a first clue as to the regions involved in
440 destabilizing the E1-P state and triggering the transition to the E2-P conformation. In the E1-P
441 tight state, the electrostatic tensions of the E1-P·ADP state are eased by rearrangements of the
442 catalytic aspartate and the surrounding side chains, likely supported by a pulling of the
443 N domain on the $D_{307}KTG$ loop as it associates with the A domain during the E1-P to E1-P
444 tight transition. This could be the main stabilizing role of the tight conformation in $KdpB_{S162\text{-}P}$
445 inhibition. Further, the structural differences in the E1-P tight state also involve a movement
446 of helix 6 in the P domain, which is not in the immediate proximity of the catalytic $KdpB_{D307}$
447 phosphate. This helix is in close proximity to the A domain and next one of the two connections
448 of the P domain to the TMD, which undergo large conformational changes during the E1/E2
449 transition. Thus, it may be an important element in signaling the ATPase to initiate the
450 transition to E2-P in the TMD from an outward- to an inward-facing state.

The regulation by inactive conformations outside the Post-Albers cycle has been postulated for other P-type ATPases (Dyla et al., 2020). Observation of translocation by the H^+ ATPase AHA2 on a single-molecule level revealed that the pump stochastically enters inactive states, from which it can return to its active form spontaneously (Veshaguri et al., 2016). These states are adopted from the E1 conformation, similar to the E1 apo tight state observed under nucleotide-free conditions for KdpFABC. However, no full inhibition in the E1-P state was observed for AHA2, indicating a different mechanism. A crystal structure of the Ca^{2+} pump SERCA was also proposed to represent a non-Post-Albers state (Dyla et al., 2020; Toyoshima et al., 2000). However, the organization of the cytosolic domains differs significantly from the tight conformation seen for KdpB, and a physiological role for this structure remains unclear. Altogether, the structural basis for KdpFABC inhibition by $KdpB_{S162}$ phosphorylation described here, describes in detail the involvement of a non-Post-Albers conformation with a clear regulatory role in P-type ATPase turnover. It extends the conformational landscape and strongly supports the emerging idea of non-catalytic off-cycle conformations with important physiological roles.

Conclusion

The data presented here illuminates the structural basis for KdpFABC inhibition by $KdpB_{S162}$ phosphorylation. We show that stalled KdpFABC adopts a novel conformation, which is either an intermediate of the E1-P/E2-P transition, or a separate state into which the A and P domains relax when the transition to the E2-P state is hindered. Moreover, the N domain in the inhibited $KdpFAB_{S162\text{-}P}C$ associates closely with the A domain in a non-Post-Albers conformation that likely further stabilizes the complex during inhibition. These results prove the involvement of off-cycle states in P-type ATPase regulation, and strongly support the burgeoning discussion of non-Post-Albers states of physiological relevance in the conformational landscapes of ion pumps. Further studies will be required to resolve how the phosphorylation of $KdpB_{S162}$ is mediated, and fully illuminate the destabilization of the E1-P state and subsequent transition to the E2-P state.

Materials and Methods

Cloning, protein production and purification

Escherichia coli kdpFABC (UniProt IDs: P36937 (KdpF), P03959 (KdpA), P03960 (KdpB), and P03961 (KdpC)) and its cysteine-free variant (provided by J.C. Greie, Osnabrück, Germany) were cloned into FX-cloning vector pBXC3H (pBXC3H was a gift from Raimund Dutzler & Eric Geertsma (Geertsma and Dutzler, 2011) (Addgene plasmid # 47068)) resulting in pBXC3H-KdpFABC and pBXC3H-KdpFABCΔCys, respectively. pBXC3H-KdpFAB$_{S162A}$C and pBXC3H-KdpFAB$_{D307N}$C were created from pBXC3H-KdpFABC by site-directed mutagenesis. Plasmids encoding variants used in EPR experiments include pBXC3H-KdpFAB$_{D307N/A407C/A494C}$CΔCys and pBXC3H-KdpFAB$_{S162A/D307N/A407C/A494C}$CΔCys, and were created by site-directed mutagenesis based on pBXC3H-KdpFABCΔCys.

KdpFABC and KdpFABC variants for structural analysis and pulsed EPR measurements were produced in *E. coli* LB2003 cells (available from the Hänelt group upon request) transformed with the respective plasmids in 12 L of KML (100 µg/ml ampicillin). Cell growth and harvesting was carried out as described previously (Stock et al., 2018). KdpFABC and KdpFABC variants were purified as previously described for wild-type KdpFABC (Stock et al., 2018).

Cryo-EM sample preparation

Wild type KdpFABC under turnover conditions

Purified wild-type KdpFABC was concentrated to 5 mg/ml and supplemented with 50 mM KCl and 2 mM ATP. The sample was incubated at room temperature for 5 min before grid preparation.

Wild type KdpFABC stabilized by orthovanadate

Purified wild-type KdpFABC was concentrated to 4 mg/ml and supplemented with 0.2 mM orthovanadate and 1 mM KCl before grid preparation.

$KdpFAB_{S162A}C$ under turnover conditions

Purified $KdpFAB_{S162A}C$, in which the inhibitory phosphorylation in KdpB is prevented by the mutation of the phosphorylated $KdpB_{S162}$ to alanine, was concentrated to 3.4 mg/ml and supplemented with 50 mM KCl and 2 mM ATP. The sample was incubated at room temperature for 5 min before grid preparation.

$KdpFAB_{D307N}C$ under nucleotide-free conditions

Purified $KdpFAB_{D307N}C$, which is prevented from progressing into an E1-P state by the mutation of the catalytic $KdpB_{D307}$ to an asparagine, was concentrated to 4 mg/ml and supplemented with 50 mM KCl before grid preparation.

Cryo-EM grid preparation

For wild-type KdpFABC with orthovanadate and nucleotide-free $KdpFAB_{D307N}C$, 2.8 µl of sample were applied to holey-carbon cryo-EM grids (Quantifoil Au R1.2/1.3, 200 mesh), which were previously glow-discharged at 5 mA for 20 s. Grids were blotted for 3 - 5 s in a Vitrobot (Mark IV, Thermo Fisher Scientific) at 20 °C and 100% humidity, and subsequently plunge-frozen in liquid propane/ethane and stored in liquid nitrogen until further use.

For the turnover samples of wild-type KdpFABC and $KdpFAB_{S162A}C$, 2.8 µl of sample were applied to holey-carbon cryo-EM grids (Quantifoil Au R1.2/1.3, 300 mesh), which were previously twice glow-discharged at 15 mA for 45 s. Grids were blotted for 2 - 6 s in a Vitrobot (Mark IV, Thermo Fisher Scientific) at 4 °C and 100% humidity, and subsequently plunge-frozen in liquid ethane and stored in liquid nitrogen until further use.

527 **Cryo-EM data collection**

528 Cryo-EM data were collected on a 200 keV Talos Arctica microscope (Thermo Fisher
529 Scientific) equipped with a post-column energy filter (Gatan) in zero-loss mode, using a 20 eV
530 slit, a 100 µm objective aperture, in an automated fashion provided by EPU software (Thermo
531 Fisher Scientific) or serialEM (Mastronarde, 2005; Schorb et al., 2019) on a K2 summit
532 detector (Gatan) in counting mode. Cryo-EM images were acquired at a pixel size of 1.012 Å
533 (calibrated magnification of 49,407×), a defocus range from -0.5 to -2 µm, an exposure time of
534 9 sec and a sub-frame exposure time of 150 ms (60 frames), and a total electron exposure on
535 the specimen level of about 52 electrons per $Å^2$. Data collection was optimized by restricting
536 the acquisition to regions displaying optimal sample thickness using an in-house written script
537 (Rheinberger et al., 2021) and data quality was monitored on-the-fly using the software
538 FOCUS (Biyani et al., 2017).

539

540 **Cryo-EM data processing**

541 For all datasets, the SBGrid (Morin et al., 2013) software package tool was used to manage the
542 software packages.

543 *$KdpFAB_{S162A}C$ under turnover conditions*

544 Pre-processing of the acquired data was performed as described above, resulting in the
545 selection of 9,170 out of 11,482 images, which were used for further analysis with the software
546 packages cryoSPARC 3.2.0 (Punjani et al., 2017) and RELION 3.1.1 (Zivanov et al., 2018).
547 First, crYOLO 1.7.6 (Wagner et al., 2019) was used to automatically pick 287,232 particles
548 using a loose threshold. Particle coordinates were imported in RELION 3.1.1 (Zivanov et al.,
549 2018), and the particles were extracted with a box size of 240 pixels. Non-protein classes were
550 removed with a single round of 2D classification in cryoSPARC 3.2.0 (Punjani et al., 2017),
551 resulting in 167,721 particles (initial particle set). These particles were then subjected to ab-

initio 3D reconstruction in cryoSPARC 3.2.0 (Punjani et al., 2017), and the best two output classes were used in subsequent jobs in an iterative way in RELION 3.1.1 (Zivanov et al., 2018). The dataset was from here on treated separately, with about 37.7% (63,240 particles) in the E2-P state and about 53.3% (89,378 particles) in the E1-P·ADP state. These particles were imported back into RELION 3.1.1, and subjected to 3D classification and refinement, against references obtained for the E1 tight and E1-P·ADP conformations. This resulted in a dataset of 46,904 particles (~28% of the initial particle set) for the E2-P conformation, and of 70,068 particles for the E1-P·ADP conformation. Several rounds of CTF refinement (Zivanov et al., 2018) were performed, using per-particle CTF estimation. The dataset for the E1-P·ADP conformation was subjected to a round of focused 3D classification with no image alignment, using a mask on the flexible A and N domains of KdpB (Hiraizumi et al., 2019). This resulted in a cleaned dataset of 58,243 particles (~35% of the initial particle set) for the E1-P·ADP state. In the last refinement iteration, a mask excluding the micelle was used and the refinement was continued until convergence (focused refinement), yielding a final map for the E2-P state at a resolution of 4.3 Å and 4.0 Å after post-processing and masking, sharpened using an isotropic b-factor of -160 Å^2. The final map for the E1-P·ADP state had a resolution of 4.0 Å after refinement and 3.7 Å after post-processing and masking, and was sharpened using an isotropic b-factor of -123 Å^2.

Wild type KdpFABC under turnover conditions

A total of 17,938 dose-fractionated cryo-EM images were recorded and subjected to motion-correction and dose-weighting of frames by MotionCor2 (Zheng et al., 2017). The CTF parameters were estimated on the movie frames by ctffind4.1.4 (Rohou and Grigorieff, 2015). Bad images showing contamination, a defocus below -0.5 or above -2.0 µm, or a bad CTF estimation were discarded, resulting in 14,604 images used for further analysis with the software packages cryoSPARC 3.2.0 (Punjani et al., 2017) and RELION 3.1.1 (Zivanov et al.,

2018). First, crYOLO 1.7.6 (Wagner et al., 2019) was used to automatically pick 1,128,433 particles using a loose threshold. Particle coordinates were imported in RELION 3.1.1 (Zivanov et al., 2018), and the particles were extracted with a box size of 240 pixels. Non-protein classes were removed with a single round of 2D classification in cryoSPARC 3.2.0 (Punjani et al., 2017), resulting in 828,847 particles (initial particle set). These particles were then subjected to ab-initio 3D reconstruction in cryoSPARC 3.2.0 (Punjani et al., 2017), and the best three output classes were used in subsequent jobs in an iterative way in RELION 3.1.1 (Zivanov et al., 2018). The dataset was from here on treated separately, with about 33.2% (275,026 particles) in the E1-P tight state and about 55.1% (346,303 and 110,601 particles) in the E1 nucleotide bound state. These particles were imported back into RELION 3.1.1, and subjected to 3D classification and refinement, against references obtained for the E1 tight and E1·ATP conformations. Several rounds of CTF refinement (Zivanov et al., 2018) were performed, using per-particle CTF estimation, before subjecting all datasets to a round of focused 3D classification with no image alignment, using a mask on the flexible A and N domains of KdpB (Hiraizumi et al., 2019). This resulted in a cleaned dataset of 114,588 particles (~14% of the initial particle set) for the E1-P tight state, and 277,912 and 80,798 for the E1 nucleotide bound conformations. The latter two were merged and subjected to several rounds of CTF refinement (Zivanov et al., 2018) using per-particle CTF estimation, before subjecting the dataset to another round of focused 3D classification with no image alignment, using a mask on the flexible A and N domains of KdpB (Hiraizumi et al., 2019). This resulted in two distinct datasets of 257,675 particles (~31% of the initial particle set) for the E1-P·ADP conformation and of 76,121 particles (~9% of the initial particle set) for the E1·ATP conformation. In the last refinement iteration, a mask excluding the micelle was used and the refinement was continued until convergence (focused refinement), yielding a final map for the E1-P tight state at a resolution of 3.7 Å and 3.4 Å after post-processing and masking, sharpened

602 using an isotropic b-factor of -134 Å^2. The final map for the E1-P·ADP state had a resolution
603 of 3.4 Å after refinement and 3.1 Å after post-processing and masking, and was sharpened
604 using an isotropic b-factor of -122 Å^2. The final map for the E1·ATP state had a resolution of
605 3.9 Å after refinement and 3.5 Å after post-processing and masking, and was sharpened using
606 an isotropic b-factor of -132 Å^2. No symmetry was imposed during 3D classification or
607 refinement.

608 *Wild type KdpFABC with orthovanadate*

609 Pre-processing of the acquired data was performed as described above, resulting in the
610 selection of 2,014 out of 2,488 images, which were used for further analysis with the software
611 package RELION 3.0.8 (Zivanov et al., 2018). First, crYOLO 1.3.1 (Wagner et al., 2019) was
612 used to automatically pick 164,891particles using a loose threshold. Particle coordinates were
613 imported in RELION 3.0.8 (Zivanov et al., 2018), and the particles were extracted with a box
614 size of 240 pixels. Non-protein classes were removed with 2D classification, resulting in
615 120,077 particles (initial particle set). For 3D classification and refinement, the map of the
616 previously generated E1 conformation EMD-0257 (Stock et al., 2018) was used as reference
617 for the first round, and the two best output classes were used in subsequent jobs in an iterative
618 way. The dataset was from here on treated separately, with about 70.9% (85,102 particles) in
619 the E1-P tight state and about 11.2% (13,508 particles) in the E2-P state. Sequentially, on the
620 E1-P tight dataset several rounds of CTF refinement, using per- particle CTF estimation, and
621 Bayesian polishing were performed (Zivanov et al., 2018), before subjecting the dataset to a
622 round of focused 3D classification with no image alignment, using a mask on the flexible A
623 and N domains of KdpB (Hiraizumi et al., 2019). This resulted in a cleaned dataset of 74,927
624 particles (~62% of the initial particle set) for the E1-P tight state, and was subjected to several
625 rounds of CTF refinement, using per-particle CTF estimation, and Bayesian polishing (Zivanov
626 et al., 2018). In the last refinement iteration, a mask excluding the micelle was used and the

refinement was continued until convergence (focused refinement), yielding a final map for the E1-P tight state at a resolution of 3.3 Å, and 3.3 Å after post-processing and masking, sharpened using an isotropic b-factor of -55 Å^2. The final map for the E2-P state (from ~11% of the initial particle set) had a resolution of 8.7 Å after refinement and 7.4 Å after post-processing and masking, and was sharpened using an isotropic b-factor of -195 Å^2. No symmetry was imposed during 3D classification or refinement.

$KdpFAB_{D307N}C$ under nucleotide-free conditions

Pre-processing of the acquired data was performed as described above, resulting in the selection of 12,864 out of 17,889 images, which were used for further analysis with the software package RELION 3.0.8 (Zivanov et al., 2018). First, crYOLO 1.3.1 (Wagner et al., 2019) was used to automatically pick 728,674 particles using a loose threshold. Particle coordinates were imported in RELION 3.0.8 (Zivanov et al., 2018), and the particles were extracted with a box size of 240 pixels. Non-protein classes were removed in several rounds of 2D classification, resulting in 469,466 particles (initial particle set). Due to the large conformational differences between both states, the full dataset was further cleaned by two independent 3D classifications against references obtained for the E1 tight state or the E1 apo open state. Particles belonging to the best classes of both runs were merged and duplicates subtracted, resulting in 306,942 particles that were subjected to a multi-reference 3D classification with no image alignment. The dataset was from here on treated separately, with about 33.7% (158,353 particles) in the E1 tight state and about 31.4% (147,589 particles) in the open state. Several rounds of CTF refinement (Zivanov et al., 2018) were performed, using per-particle CTF estimation, before subjecting both datasets to a round of focused 3D classification with no image alignment, using a mask on the flexible A and N domains of KdpB (Hiraizumi et al., 2019). This resulted in a cleaned dataset of 88,852 particles (~19% of the initial particle set) for the E1 tight state, 75,711 particles (~16% of the initial particle set) for

652 the E1 apo open state 1, and 47,981 particles (~10% of the initial particle set) for the E1 apo
653 open state 2. In the last refinement iteration, a mask excluding the micelle was used and the
654 refinement was continued until convergence (focused refinement), yielding a final map for the
655 E1 tight state at a resolution of 3.8 Å and 3.4 Å after post-processing and masking, sharpened
656 using an isotropic b-factor of -113 Å^2. The final map for the E1 apo open state 1 had a resolution
657 of 3.9 Å after refinement and 3.5 Å after post-processing and masking, and was sharpened
658 using an isotropic b-factor of -117 Å^2. The final map for the E1 apo open state 2 had a resolution
659 of 4.0 Å after refinement and 3.7 Å after post-processing and masking, and was sharpened
660 using an isotropic b-factor of -119 Å^2. For 3D classification and refinement, the map of the
661 previously generated E1 conformation [EMD-0257] (Stock et al., 2018) was used as reference
662 for the first round, and the best output class was used in subsequent jobs in an iterative way.
663 For all datasets, local resolution estimates were calculated by RELION and no symmetry was
664 imposed during 3D classification or refinement. All resolutions were estimated using the 0.143
665 cut-off criterion (Rosenthal and Henderson, 2003) with gold-standard Fourier shell correlation
666 (FSC) between two independently refined half maps. During post-processing, the approach of
667 high-resolution noise substitution was used to correct for convolution effects of real-space
668 masking on the FSC curve (Chen et al., 2013).
669
670 **Model building and validation**
671 Available KdpFABC structures like E1·ATP conformation [7NNL], E1 [6HRA] and E2
672 conformation [6HRB] were docked into the obtained cryo-EM maps using UCSF Chimera
673 (Pettersen et al., 2004) and used as initial models. Wherever required, rigid body movements
674 were applied to accommodate for conformational changes, and models were subjected to an
675 iterative process of real space refinement using Phenix.real_space_refinement with secondary
676 structure restraints (Afonine et al., 2018; Liebschner et al., 2019) followed by manual

677 inspection and adjustments in Coot (Emsley and Cowtan, 2004). K^+ ions, cardiolipin, ATP,
678 ADP, P_i, and orthovanadate were modelled into the cryo-EM maps in Coot. The final models
679 were refined in real space with Phenix.real_space_refinement with secondary structure
680 restraints (Afonine et al., 2018; Liebschner et al., 2019). For validation of the refinement, FSCs
681 (FSC_{sum}) between the refined models and the final maps were determined. To monitor the
682 effects of potential over-fitting, random shifts (up to 0.5 Å) were introduced into the
683 coordinates of the final model, followed by refinement against the first unfiltered half-map.
684 The FSC between this shaken-refined model and the first half-map used during validation
685 refinement is termed FSC_{work}, and the FSC against the second half-map, which was not used at
686 any point during refinement, is termed FSC_{free}. The marginal gap between the curves describing
687 FSC_{work} and FSC_{free} indicate no over-fitting of the model. The geometries of the atomic models
688 were evaluated by MolProbity (Williams et al., 2018).
689
690 **EPR sample purification, preparation, data acquisition and analysis**
691 $KdpFAB_{A407C/A494C}C\Delta Cys$, $KdpFAB_{D307N/A407C/A494C}C\Delta Cys$ and
692 $KdpFAB_{S162A/D307N/A407C/A494C}C\Delta Cys$, variants based on an otherwise Cys-less background,
693 were produced and purified as described for $KdpFAB_{G150C/A407C}C\Delta Cys$ (Stock et al., 2018).
694 Purified and spin-labeled KdpFABCΔCys variants were concentrated to 4 - 7 mg ml^{-1} and
695 supplemented with 14% deuterated glycerol (v/v) and 50 mM KCl. 5 mM AMPPCP stabilizing
696 the E1-ATP conformations was added when indicated.
697 Pulsed EPR measurements were performed at Q band (34 GHz) and -223 °C on an ELEXSYS-
698 E580 spectrometer (Bruker). For this, 15 µl of the freshly prepared samples were loaded into
699 EPR quartz tubes with a 1.6 mm outer diameter and shock frozen in liquid nitrogen. During
700 the measurements, the temperature was controlled by the combination of a continuous-flow
701 helium cryostat (Oxford Instruments) and a temperature controller (Oxford Instruments). The

four-pulse DEER sequence was applied (Pannier et al., 2011) with observer pulses of 32 ns and a pump pulse of 12 - 14 ns. The frequency separation was set to 70 MHz and the frequency of the pump pulse to the maximum of the nitroxide EPR spectrum. Validation of the distance distributions was performed by means of the validation tool included in DeerAnalysis (Jeschke et al., 2006) and varying the parameters "Background start" and "Background density" in the suggested range by applying fine grid. A prune level of 1.15 was used to exclude poor fits. Furthermore, interspin distance predictions were carried out by using the rotamer library approach included in the MMM software package (Jeschke, 2018; Polyhach et al., 2010). The calculation of the interspin distance predictions is based on the cryo-EM structures of the E1 tight, E1 apo open, and E1·ATP conformations for the comparison with the experimentally determined interspin distance distributions.

Molecular dynamics simulations

Molecular dynamics (MD) simulations were built using the coordinates of eight states of the complex (see Table 3). To reduce the size of the simulation box, KdpA and KdpC were removed from the system, as these were considered unlikely to impact the dynamics of the N, P, and A domains in the timescales simulated. The systems were described with the CHARMM36m force field (Best et al., 2012; Huang et al., 2016) and built into POPE membranes with TIP3P waters and K^+ and Cl^- to 150 mM, using CHARMM-GUI (Jo et al., 2007; Lee et al., 2016). Where present, $KdpB_{S162}$ was phosphorylated for each system, and for the E1·ATP and E1-P·ADP states, the nucleotide was included based on the structural coordinates. Where present, the K^+ bound in the CBS was preserved.

Each system was minimized using the steepest descents method, then equilibrated with positional restraints on heavy atoms for 100 ps in the NPT ensemble at 310 K with the V-rescale thermostat and a 1 ps coupling time constant, and semi-isotropic Parrinello-Rahman

pressure coupling at 1 atm, with a 5 ps coupling time constant (Bussi et al., 2007; Parrinello and Rahman, 1981). Production simulations were run using 2 fs time steps over 50 ns, with 3 repeats run for each state. The simulations were kept relatively short to preserve the conformation of the input structures, whilst allowing sufficient conformational flexibility to sample the side chain motions and rearrangements within the given state. Removal of KdpA and KdpC did not appear to reduce the stability of KdpBF, as all systems had moderate-low backbone RMSDs at the end of the simulations (see Table 3).

Table 2: Details of MD simulations run. All simulations were run in POPE membranes, over 3 x 50 ns. RMSDs are the mean and standard deviations over three repeats.

State	RMSD (nm)
E1 apo open 1 (nucleotide-free)	0.47 ± 0.09 nm
E1 apo open 2 (nucleotide-free)	0.55 ± 0.12 nm
E1 apo tight (nucleotide-free)	0.32 ± 0.08 nm
E1·ATP_{early} (turnover WT)	0.35 ± 0.04 nm
E1-P·ADP (turnover WT)	0.51 ± 0.04 nm
E1-P·ADP (turnover $KdpB_{S162A}$)	0.30 ± 0.06 nm
E1-P tight (turnover WT)	0.31 ± 0.04 nm
E1-P tight (orthovanadate)	0.27 ± 0.03 nm

Contact analysis was performed by counting the number of residues from each domain which were within 0.4 nm of a residue from a different domain, for every frame over 3 x 50 ns simulation. The domains were defined as the following residues of KdpB: A domain = 89 - 214, N domain = 314 - 450, P-domain = 277 - 313 and 451 - 567. Contact analysis was run with the Gromacs tool gmx select.

High-frequency contacting residue pairs were identified as any pair of residues in contact for at least 90% of frames over 3 x 50 ns of simulation time. Analyses were run using MDAnalysis (Michaud-Agrawal et al., 2011) and plotted using NumPy (Harris et al., 2020) and Matplotlib (Hunter, 2007).

All simulations were run in Gromacs 2019 (Berendsen et al., 1995).

Figure preparation

All figures were prepared using USCF Chimera (Pettersen et al., 2004), UCSF ChimeraX (Pettersen et al., 2021), VMD (Humphrey et al., 1996), OriginPro 2016, and GraphPad Prism 8 and 9.

Data availability

Data supporting the findings of this manuscript are available from the corresponding authors upon request. The three-dimensional cryo-EM densities and corresponding modelled coordinates of KdpFABC have been deposited in the Electron Microscopy Data Bank and the Protein Data Bank under the accession numbers summarized in Table 3. The depositions include maps calculated with higher b-factors, both half-maps and the mask used for the final FSC calculation.

Table 3: EMDB and PDB accession codes of structure depositions.

State	EMDB #	PDB #
E1·ATP_{early} (turnover WT)	EMD-14913	7ZRG
E1-P·ADP (turnover WT)	EMD-14917	7ZRK
E1-P tight (turnover WT)	EMD-14912	7ZRE
E1-P tight (orthovanadate)	EMD-14911	7ZRD
E2-P (orthovanadate)	EMD-14347	N/A
E1-P·ADP (turnover $KdpB_{S162A}$)	EMD-14919	7ZRM
E2-P (turnover $KdpB_{S162A}$)	EMD-14918	7ZRL
E1 apo tight (nucleotide-free $KdpB_{D307N}$)	EMD-14914	7ZRH
E1 apo open 1 (nucleotide-free $KdpB_{D307N}$)	EMD-14915	7ZRI
E1 apo open 2 (nucleotide-free $KdpB_{D307N}$)	EMD-14916	7ZRJ

763 **Table 4: Key resources table.**

Reagent type (species) or resource	Designation	Source or reference	Identifiers	Additional information
Gene (*Escherichia coli*)	*kdpFABC*		Uniprot IDs:	
			kdpF: P36937	
			kdpA: P03959	
			kdpB: P03960	
			kdpC: P03961	
Plasmid (backbone)	*pBXC3H*	doi: 10.1007/978-1-62703-764-8_11	Addgene catalog #47068	
Strain, strain background (*Escherichia coli)*	LB2003 *(F⁻ thi metE rpsL gal rha kup1 ΔkdpFABC5 ΔtrkA*)	doi: 10.1007/s002030050425		
Sequence-based reagent	*kdpB_S162A_for*	Eurofins Genomics (Luxembourg)		5'-GCGCCATCACCGGGGAAGCGGCACC-3'
Sequence-based reagent	*kdpB_S162A_for*	Eurofins Genomics (Luxembourg)		5'-ACCGGTGCCGCTTCCCCGGTGATGG-3'
Sequence-based reagent	*kdpB_D307N_for*	Eurofins Genomics (Luxembourg)		5'-GCTACTGAATAAAACCGGCACCATCAC-3'
Sequence-based reagent	*kdpB_D307N_rev*	Eurofins Genomics (Luxembourg)		5'-GGTGCCGGTTTTATTCAGTAGCAGAACG-3'
Sequence-based reagent	*kdpB_A407C_for*	Eurofins Genomics (Luxembourg)		5'-CATTCGTCGCCATGTTGAGTGTAACGG-3'
Sequence-based reagent	*kdpB_A407C_rev*	Eurofins Genomics (Luxembourg)		5'-CGTTACACTCAACATGGCGACGAATGG-3'
Sequence-based reagent	*kdpB_A494C_for*	Eurofins Genomics (Luxembourg)		5'-GATTTTCTCGCCGAATGTACACCGGAGGCC-3'
Sequence-based reagent	*kdpB_A494C_rev*	Eurofins Genomics (Luxembourg)		5'-GGCCTCCGGTGTACATTCGGCGAGAAAATC-3'

EPR spin label	MTSSL	Toronto Research Chemicals Inc., North York, Canada		
Reagent	Orthovanadate	Merck KGaA, Darmstadt, Germany		
Reagent	Adenosine 5’-triphosphate	Merck KGaA, Darmstadt, Germany		
Software	DeerAnalysis	doi: 10.1007/BF03166213		
Other (Cryo-EM Grids)	200 and 300 mesh Au R1.2/1.3 cryo-EM grids	Quantifoil, Großlöbichau, Germany		
Software, algorithm	EPU v 2.3	Thermo Fisher (Eindhoven, Netherlands) https://www.thermofisher.com/nl/en/home/electron-microscopy/products/software-em-3d-vis/epu-software.html		
Software, algorithm	Sample thickness measurement script	https://doi.org/10.1101/2020.12.01.392100		
Software, algorithm	Focus	https://doi.org/10.1016/j.jsb.2017.03.007 https://focus.c-cina.unibas.ch/about.php		
Software, algorithm	SBGrid	https://doi.org/10.7554/eLife.01456 https://sbgrid.org/software/		
Software, algorithm	MotionCor2	https://doi.org/10.1038/nmeth.4193 http://msg.ucsf.edu/em/software/motioncor2.html		
Software, algorithm	Ctffind 4.1.13	https://doi.org/10.1016/j.jsb.2015.08.008 http://grigoriefflab.janelia.org/ctf		
Software, algorithm	Ctffind 4.1.14	https://doi.org/10.1016/j.jsb.2015.08.008 http://grigoriefflab.janelia.org/ctf		

Software, algorithm	crYOLO 1.3.1	https://doi.org/10.1038/s42003-019-0437-z https://cryolo.readthedocs.io/en/stable/#		
Software, algorithm	crYOLO 1.7.6	https://doi.org/10.1038/s42003-019-0437-z https://cryolo.readthedocs.io/en/stable/#		
Software, algorithm	cryoSPARC 3.2.0	https://doi.org/10.1038/nmeth.4169 https://cryosparc.com		
Software, algorithm	RELION 3.0.8	https://doi.org/10.7554/eLife.42166 https://www2.mrc-lmb.cam.ac.uk/relion/		
Software, algorithm	RELION 3.1.1	https://doi.org/10.7554/eLife.42166 https://www2.mrc-lmb.cam.ac.uk/relion/		
Software, algorithm	Coot 0.9	https://doi.org/10.1107/S0907444904019158 https://www2.mrc-lmb.cam.ac.uk/personal/pemsley/coot/		
Software, algorithm	Phenix 1.19.2	https://doi.org/10.1107/S0907444904019158 http://phenix-online.org/		
Software, algorithm	Molprobity 4.5.1	https://doi.org/10.1002/pro.3330 http://molprobity.biochem.duke.edu		
Software, algorithm	UCSF Chimera 1.15	https://doi.org/10.1002/jcc.20084 https://www.cgl.ucsf.edu/chimera/		
Software, algorithm	UCSF Chimerax 1.1.1	https://doi.org/10.1002/pro.3943 https://www.rbvi.ucsf.edu/chimerax/		
Software, algorithm	Origin Pro 2016	OriginLab https://www.originlab.com/2016		

Software, algorithm	Gromacs 2019.4	https://doi.org/10.1016/0010-4655(95)00042-E https://www.gromacs.org/		
Software, algorithm	VMD 1.9.4a12	https://doi.org/10.1016/0263-7855(96)00018-5 http://www.ks.uiuc.edu/Research/vmd/		
Software, algorithm	charmm-gui	https://doi.org/10.1021/acs.jctc.5b00935 http://www.charmm-gui.org/		
Software, algorithm	MDAnalysis 1.0.1	https://doi.org/10.1002/jcc.21787 https://www.mdanalysis.org/		
Software, algorithm	NumPy 1.20.0	https://doi.org/10.1038/s41586-020-2649-2 https://numpy.org/		
Software, algorithm	matplotlib 3.3.4	https://doi.org/10.1109/MCSE.2007.55 https://matplotlib.org/		
Software, algorithm	GraphPad Prism 8 and 9	https://www.graphpad.com/scientific-software/prism/		

764

Acknowledgements

CP thanks Michiel Punter for IT support. JMS thanks Paul J.N. Böhm for assistance with cloning and cell growth. PJS acknowledges the University of Warwick Scientific Computing Research Technology Platform for computational access. The electron microscopy within this work is part of the research program National Roadmap for Large-Scale Research Infrastructure (NEMI), project number 184.034.014, which is financed by the Dutch Research Council (NWO).

Competing interest

No conflict of interest

Author contributions

Jakob M Silberberg: Validation, Formal analysis, Investigation, writing - original draft, writing – review & editing, visualization

Charlott Stock: Validation, Formal analysis, Investigation, writing - original draft, writing – review & editing, visualization

Lisa Hielkema: Validation, Formal analysis, Investigation, writing - original draft, writing – review & editing, visualization

Robin A Corey: Validation, Formal analysis, Investigation, writing - original draft, writing – review & editing, visualization

Dorith Wunnicke: Validation, Formal analysis, Investigation

Jan Rheinberger: Validation, Formal analysis, Investigation

Victor RA Dubach: Validation, Formal analysis, Investigation

Phillip J Stansfeld: Conceptualization, Writing – review & editing, Supervision, Project administration, Funding acquisition

Inga Hänelt: Conceptualization, Writing – review & editing, Supervision, Project administration, Funding acquisition

Cristina Paulino: Conceptualization, Writing – review & editing, Supervision, Project administration, Funding acquisition

Funding

The work was funded by the NWO Veni grant (722.017.001) and the NWO Start-Up grant (740.018.016) to CP as well as by the DFG Emmy Noether grant (HA6322/3-1), the Heisenberg program (HA6322/5-1) and the Life Science Bridge Award by the Aventis Foundation to IH. Research in PJS's lab is funded by Wellcome (208361/Z/17/Z), the MRC (MR/S009213/1) and BBSRC (BB/P01948X/1, BB/R002517/1 and BB/S003339/1). JMS is funded by the State of Hesse in the LOEWE Schwerpunkt TRABITA and RAC is funded by Wellcome (208361/Z/17/Z). This project made use of time on ARCHER, ARCHER2 and JADE granted via the UK High-End Computing Consortium for Biomolecular Simulation, HECBioSim (http://hecbiosim.ac.uk), supported by EPSRC (grant no. EP/R029407/1). PJS thanks the Warwick Scientific Computing Research Technology platform for computational access.

804 **References**

805 Afonine P V, Poon BK, Read RJ, Sobolev O V, Terwilliger TC, Urzhumtsev A, Adams PD.
806 2018. Real-space refinement in PHENIX for cryo-EM and crystallography. *Acta*
807 *Crystallogr Sect D Struct Biol* **74**:531–544. doi:10.1107/S2059798318006551

808 Albers RW. 1967. Biochemical Aspects of Active Transport. *Annu Rev Biochem* **36**:727–756.
809 doi:10.1146/annurev.bi.36.070167.003455

810 Altendorf K, Gassel M, Puppe W, Möllenkamp T, Zeeck A, Boddien C, Fendler K, Bamberg
811 E, Dröse S. 1998. Structure and function of the Kdp-ATPase of *Escherichia coli*. *Acta*
812 *Physiol Scand Suppl* **643**:137–46.

813 Berendsen HJC, van der Spoel D, van Drunen R. 1995. GROMACS: A message-passing
814 parallel molecular dynamics implementation. *Comput Phys Commun* **91**:43–56.
815 doi:10.1016/0010-4655(95)00042-E

816 Best RB, Zhu X, Shim J, Lopes PEM, Mittal J, Feig M, MacKerell AD. 2012. Optimization
817 of the additive CHARMM all-atom protein force field targeting improved sampling of
818 the backbone φ, ψ and side-chain χ1 and χ2 Dihedral Angles. *J Chem Theory Comput*
819 **8**:3257–3273. doi:10.1021/ct300400x

820 Biyani N, Righetto RD, McLeod R, Caujolle-Bert D, Castano-Diez D, Goldie KN, Stahlberg
821 H. 2017. Focus: The interface between data collection and data processing in cryo-EM.
822 *J Struct Biol* **198**:124–133. doi:10.1016/j.jsb.2017.03.007

823 Bublitz M, Poulsen H, Morth JP, Nissen P. 2010. In and out of the cation pumps: P-Type
824 ATPase structure revisited. *Curr Opin Struct Biol* **20**:431–439.
825 doi:10.1016/j.sbi.2010.06.007

826 Bussi G, Donadio D, Parrinello M. 2007. Canonical sampling through velocity rescaling. *J*
827 *Chem Phys* **126**:014101. doi:10.1063/1.2408420

828 Chen S, McMullan G, Faruqi AR, Murshudov GN, Short JM, Scheres SHW, Henderson R.
829 2013. High-resolution noise substitution to measure overfitting and validate resolution in
830 3D structure determination by single particle electron cryomicroscopy. *Ultramicroscopy*
831 **135**:24–35. doi:10.1016/j.ultramic.2013.06.004

832 Clausen JD, Bublitz M, Arnou B, Olesen C, Andersen JP, Møller JV, Nissen P. 2016. Crystal
833 Structure of the Vanadate-Inhibited Ca^{2+}-ATPase. *Structure* **24**:617–623.
834 doi:10.1016/j.str.2016.02.018

835 Damnjanovic B, Weber A, Potschies M, Greie J-C, Apell H-J. 2013. Mechanistic Analysis of
836 the Pump Cycle of the KdpFABC P-Type ATPase. *Biochemistry* **52**:5563–5576.
837 doi:10.1021/bi400729e

838 Diskowski M, Mikusevic V, Stock C, Hänelt I. 2015. Functional diversity of the superfamily
839 of K^+ transporters to meet various requirements. *Biol Chem*. doi:10.1515/hsz-2015-0123

840 Dubey V, Stokes DL, Pedersen BP, Khandelia H. 2021. An Intracellular Pathway Controlled
841 by the N-terminus of the Pump Subunit Inhibits the Bacterial KdpFABC Ion Pump in
842 High K^+ Conditions. *J Mol Biol* **433**:167008. doi:10.1016/j.jmb.2021.167008

843 Durell SR, Bakker EP, Guy HR. 2000. Does the KdpA subunit from the high affinity K^+-
844 translocating P-type Kdp-ATPase have a structure similar to that of K^+ channels?
845 *Biophys J* **78**:188–99. doi:10.1016/S0006-3495(00)76584-2

846 Dyla M, Kjærgaard M, Poulsen H, Nissen P. 2020. Structure and Mechanism of P-Type

847 ATPase Ion Pumps. *Annu Rev Biochem* **89**. doi:10.1146/annurev-biochem-010611-
848 112801

849 Emsley P, Cowtan K. 2004. Coot: Model-building tools for molecular graphics. *Acta*
850 *Crystallogr Sect D Biol Crystallogr* **60**:2126–2132. doi:10.1107/S0907444904019158

851 Epstein W, Buurman E, McLaggan D, Naprstek J. 1993. Multiple mechanisms, roles and
852 controls of K^+ transport in *Escherichia coli*. *Biochemical Society Transactions* pp.
853 1006–1010. doi:10.1042/bst0211006

854 Gaßel M, Möllenkamp T, Puppe W, Altendorf K. 1999. The KdpF subunit is part of the K^+-
855 translocating Kdp complex of *Escherichia coli* and is responsible for stabilization of the
856 complex in vitro. *J Biol Chem* **274**:37901–37907. doi:10.1074/jbc.274.53.37901

857 Geertsma ER, Dutzler R. 2011. A versatile and efficient high-throughput cloning tool for
858 structural biology. *Biochemistry* **50**:3272–3278. doi:10.1021/bi200178z

859 Harris CR, Millman KJ, van der Walt SJ, Gommers R, Virtanen P, Cournapeau D, Wieser E,
860 Taylor J, Berg S, Smith NJ, Kern R, Picus M, Hoyer S, van Kerkwijk MH, Brett M,
861 Haldane A, del Río JF, Wiebe M, Peterson P, Gérard-Marchant P, Sheppard K, Reddy
862 T, Weckesser W, Abbasi H, Gohlke C, Oliphant TE. 2020. Array programming with
863 NumPy. *Nature*. doi:10.1038/s41586-020-2649-2

864 Hesse JE, Wieczorek L, Altendorf K, Reicin AS, Dorus E, Epstein W. 1984. Sequence
865 homology between two membrane transport ATPases, the Kdp-ATPase of *Escherichia*
866 *coli* and the Ca^{2+}-ATPase of sarcoplasmic reticulum. *Proc Natl Acad Sci U S A*
867 **81**:4746–4750. doi:10.1073/pnas.81.15.4746

868 Hiraizumi M, Yamashita K, Nishizawa T, Nureki O. 2019. Cryo-EM structures capture the
869 transport cycle of the P4-ATPase flippase. *Science* **365**:1149–1155.
870 doi:10.1126/science.aay3353

871 Huang C-S, Panyella Pedersen B, Stokes DL. 2017. Crystal structure of the potassium-
872 importing KdpFABC membrane complex. *Nature* **546**:681–685.
873 doi:10.1038/nature22970

874 Huang J, Rauscher S, Nawrocki G, Ran T, Feig M, De Groot BL, Grubmüller H, MacKerell
875 AD. 2016. CHARMM36m: an improved force field for folded and intrinsically
876 disordered proteins. *Nat Methods 2016 141* **14**:71–73. doi:10.1038/nmeth.4067

877 Humphrey W, Dalke A, Schulten K. 1996. VMD: Visual molecular dynamics. *J Mol Graph*
878 **14**:33–38. doi:10.1016/0263-7855(96)00018-5

879 Hunter JD. 2007. Matplotlib: A 2D graphics environment. *Comput Sci Eng* **9**:90–95.
880 doi:10.1109/MCSE.2007.55

881 Jeschke G. 2018. MMM: A toolbox for integrative structure modeling. *Protein Sci* **27**:76–85.
882 doi:10.1002/pro.3269

883 Jeschke G, Chechik V, Ionita P, Godt A, Zimmermann H, Banham J, Timmel CR, Hilger D,
884 Jung H. 2006. Applied Magnetic Resonance DeerAnalysis2006 -a Comprehensive
885 Software Package for Analyzing Pulsed ELDOR Data. *Appl Magn Reson* **30**:473–498.

886 Jo S, Kim T, Im W. 2007. Automated Builder and Database of Protein/Membrane Complexes
887 for Molecular Dynamics Simulations. *PLoS One* **2**:e880.
888 doi:10.1371/journal.pone.0000880

889 Lee J, Cheng X, Swails JM, Yeom MS, Eastman PK, Lemkul JA, Wei S, Buckner J, Jeong
890 JC, Qi Y, Jo S, Pande VS, Case DA, Brooks CL, MacKerell AD, Klauda JB, Im W.

2016. CHARMM-GUI Input Generator for NAMD, GROMACS, AMBER, OpenMM, and CHARMM/OpenMM Simulations Using the CHARMM36 Additive Force Field. *J Chem Theory Comput* **12**:405–413. doi:10.1021/acs.jctc.5b00935

Liebschner D, Afonine P V., Baker ML, Bunkoczi G, Chen VB, Croll TI, Hintze B, Hung LW, Jain S, McCoy AJ, Moriarty NW, Oeffner RD, Poon BK, Prisant MG, Read RJ, Richardson JS, Richardson DC, Sammito MD, Sobolev O V., Stockwell DH, Terwilliger TC, Urzhumtsev AG, Videau LL, Williams CJ, Adams PD. 2019. Macromolecular structure determination using X-rays, neutrons and electrons: Recent developments in Phenix. *Acta Crystallogr Sect D Struct Biol* **75**:861–877. doi:10.1107/S2059798319011471

Mastronarde DN. 2005. Automated electron microscope tomography using robust prediction of specimen movements. *J Struct Biol* **152**:36–51. doi:10.1016/j.jsb.2005.07.007

Michaud-Agrawal N, Denning EJ, Woolf TB, Beckstein O. 2011. MDAnalysis: A toolkit for the analysis of molecular dynamics simulations. *J Comput Chem* **32**:2319–2327. doi:10.1002/jcc.21787

Morin A, Eisenbraun B, Key J, Sanschagrin PC, Timony MA, Ottaviano M, Sliz P. 2013. Collaboration gets the most out of software. *eLife* **2**:e01456. doi:10.7554/eLife.01456

Pannier M, Veit S, Godt A, Jeschke G, Spiess HW. 2011. Dead-time free measurement of dipole–dipole interactions between electron spins. *J Magn Reson* **213**:316–325. doi:10.1016/j.jmr.2011.08.035

Parrinello M, Rahman A. 1981. Polymorphic transitions in single crystals: A new molecular dynamics method. *J Appl Phys* **52**:7182–7190. doi:10.1063/1.328693

Pedersen BP, Stokes DL, Apell HJ. 2019. The KdpFABC complex–K^+ transport against all odds. *Mol Membr Biol*. doi:10.1080/09687688.2019.1638977

Pettersen EF, Goddard TD, Huang CC, Couch GS, Greenblatt DM, Meng EC, Ferrin TE. 2004. UCSF Chimera - A visualization system for exploratory research and analysis. *J Comput Chem* **25**:1605–1612. doi:10.1002/jcc.20084

Pettersen EF, Goddard TD, Huang CC, Meng EC, Couch GS, Croll TI, Morris JH, Ferrin TE. 2021. UCSF ChimeraX: Structure visualization for researchers, educators, and developers. *Protein Sci* **30**:70–82. doi:10.1002/pro.3943

Polarek JW, Williams G, Epstein W. 1992. The products of the *kdpDE* operon are required for expression of the Kdp ATPase of *Escherichia coli*. *J Bacteriol* **174**:2145–2151. doi:10.1128/jb.174.7.2145-2151.1992

Polyhach Y, Bordignon E, Jeschke G. 2010. Rotamer libraries of spin labelled cysteines for protein studies. *Phys Chem Chem Phys* **13**:2356–2366. doi:10.1039/c0cp01865a

Post RL, Hegyvary C, Kume S. 1972. Activation by adenosine triphosphate in the phosphorylation kinetics of sodium and potassium ion transport adenosine triphosphatase. *J Biol Chem* **247**:6530–6540.

Punjani A, Rubinstein JL, Fleet DJ, Brubaker MA. 2017. CryoSPARC: Algorithms for rapid unsupervised cryo-EM structure determination. *Nat Methods* **14**:290–296. doi:10.1038/nmeth.4169

Rheinberger J, Oostergetel G, Resch GP, Paulino C. 2021. Optimized cryo-EM data-acquisition workflow by sample-thickness determination. *Acta Crystallogr Sect D Struct Biol* **77**:565–571. doi:10.1107/S205979832100334X

935 Rhoads DB, Epstein W. 1977. Energy coupling to Net K^+ transport in *Escherichia coli* K 12.
936 *J Biol Chem* **252**:1394–1401. doi:10.1016/s0021-9258(17)40669-7

937 Roe AJ, McLaggan D, O'Byrne CP, Booth IR. 2000. Rapid inactivation of the *Escherichia*
938 *coli* Kdp K^+ uptake system by high potassium concentrations. *Mol Microbiol* **35**:1235–
939 1243. doi:10.1046/J.1365-2958.2000.01793.X

940 Rohou A, Grigorieff N. 2015. CTFFIND4: Fast and accurate defocus estimation from
941 electron micrographs. *J Struct Biol* **192**:216–221. doi:10.1016/j.jsb.2015.08.008

942 Rosenthal PB, Henderson R. 2003. Optimal determination of particle orientation, absolute
943 hand, and contrast loss in single-particle electron cryomicroscopy. *J Mol Biol* **333**:721–
944 745. doi:10.1016/j.jmb.2003.07.013

945 Schniederberend M, Zimmann P, Bogdanov M, Dowhan W, Altendorf K. 2010. Influence of
946 K^+-dependent membrane lipid composition on the expression of the *kdpFABC* operon in
947 *Escherichia coli*. *Biochim Biophys Acta - Biomembr* **1798**:32–39.
948 doi:10.1016/j.bbamem.2009.10.002

949 Schorb M, Haberbosch I, Hagen WJH, Schwab Y, Mastronarde DN. 2019. Software tools for
950 automated transmission electron microscopy. *Nat Methods* **16**:471–477.
951 doi:10.1038/s41592-019-0396-9

952 Silberberg JM, Corey RA, Hielkema L, Stock C, Stansfeld PJ, Paulino C, Hänelt I. 2021.
953 Deciphering ion transport and ATPase coupling in the intersubunit tunnel of KdpFABC.
954 *Nat Commun* **12**. doi:10.1038/S41467-021-25242-X

955 Sørensen TLM, Møller JV, Nissen P. 2004. Phosphoryl transfer and calcium ion occlusion in
956 the calcium pump. *Science* **304**:1672–1675. doi:10.1126/science.1099366

957 Stautz J, Hellmich Y, Fuss MF, Silberberg JM, Devlin JR, Stockbridge RB, Hänelt I. 2021.
958 Molecular mechanisms for bacterial potassium homeostasis. *J Mol Biol* 166968.
959 doi:10.1016/j.jmb.2021.166968

960 Stock C, Hielkema L, Tascón I, Wunnicke D, Oostergetel GT, Azkargorta M, Paulino C,
961 Hänelt I. 2018. Cryo-EM structures of KdpFABC suggest a K^+ transport mechanism via
962 two inter-subunit half-channels. *Nat Commun* **9**:4971. doi:10.1038/s41467-018-07319-2

963 Sweet ME, Larsen C, Zhang X, Schlame M, Pedersen BP, Stokes DL. 2021. Structural basis
964 for potassium transport in prokaryotes by KdpFABC. *Proc Natl Acad Sci* **118**.

965 Sweet ME, Zhang X, Erdjument-Bromage H, Dubey V, Khandelia H, Neubert TA, Pedersen
966 BP, Stokes DL. 2020. Serine phosphorylation regulates the P-type potassium pump
967 KdpFABC. *eLife* **9**:e55480. doi:10.7554/eLife.55480

968 Toyoshima C, Nakasako M, Nomura H, Ogawa H. 2000. Crystal structure of the calcium
969 pump of sarcoplasmic reticulum at 2.6 Å resolution. *Nature* **405**:647–655.
970 doi:10.1038/35015017

971 Veshaguri S, Christensen SM, Kemmer GC, Ghale G, Møller MP, Lohr C, Christensen AL,
972 Justesen BH, Jørgensen IL, Schiller J, Hatzakis NS, Grabe M, Günther Pomorski T,
973 Stamou D. 2016. Direct observation of proton pumping by a eukaryotic P-type ATPase.
974 *Science* **351**:1469–1473. doi:10.1126/science.aad6429

975 Wagner T, Merino F, Stabrin M, Moriya T, Antoni C, Apelbaum A, Hagel P, Sitsel O, Raisch
976 T, Prumbaum D, Quentin D, Roderer D, Tacke S, Siebolds B, Schubert E, Shaikh TR,
977 Lill P, Gatsogiannis C, Raunser S. 2019. SPHIRE-crYOLO is a fast and accurate fully
978 automated particle picker for cryo-EM. *Commun Biol* **2**. doi:10.1038/s42003-019-0437-

z

Williams CJ, Headd JJ, Moriarty NW, Prisant MG, Videau LL, Deis LN, Verma V, Keedy DA, Hintze BJ, Chen VB, Jain S, Lewis SM, Arendall WB, Snoeyink J, Adams PD, Lovell SC, Richardson JS, Richardson DC. 2018. MolProbity: More and better reference data for improved all-atom structure validation. *Protein Sci* **27**:293–315. doi:10.1002/pro.3330

Zheng SQ, Palovcak E, Armache JP, Verba KA, Cheng Y, Agard DA. 2017. MotionCor2: Anisotropic correction of beam-induced motion for improved cryo-electron microscopy. *Nat Methods*. doi:10.1038/nmeth.4193

Zivanov J, Nakane T, Forsberg BO, Kimanius D, Hagen WJH, Lindahl E, Scheres SHW. 2018. New tools for automated high-resolution cryo-EM structure determination in RELION-3. *eLife* **7**:e42166. doi:10.7554/eLife.42166

Supplementary Data

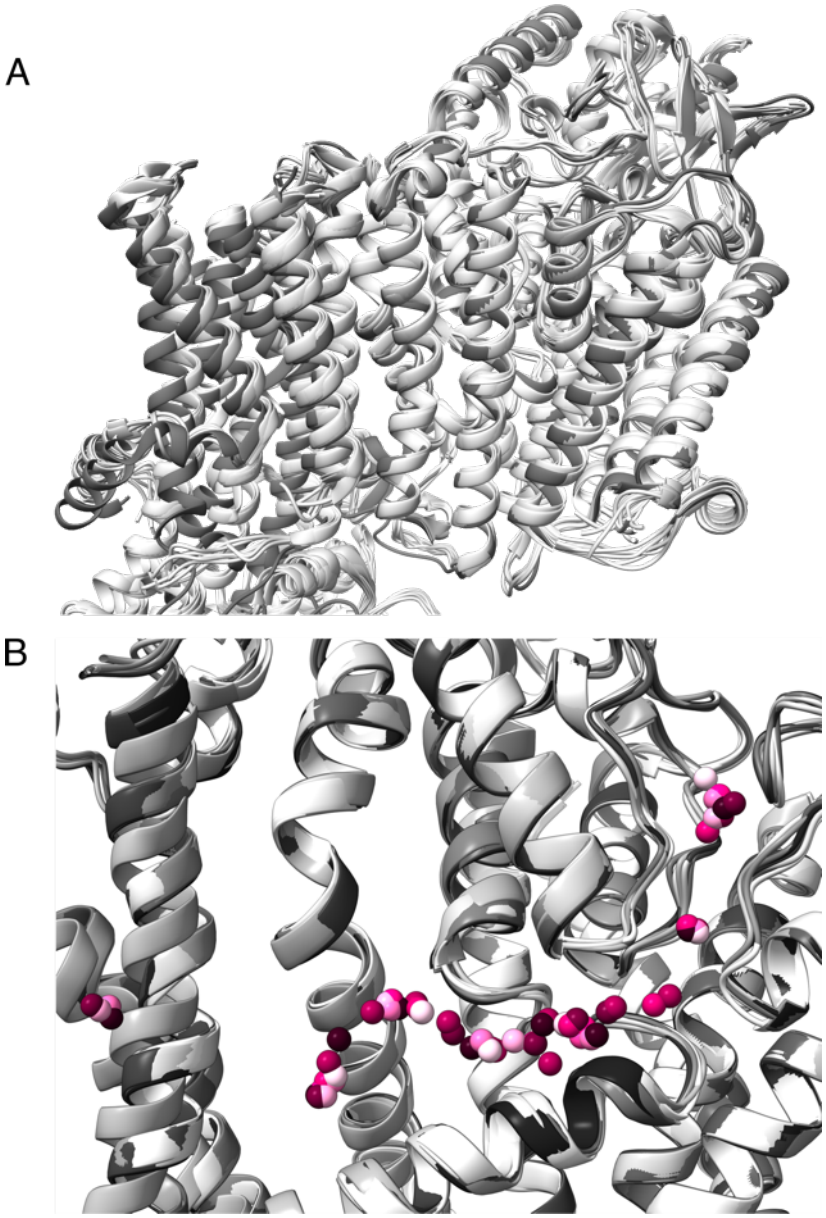

Table 1 – Figure Supplement 1: Comparison of TMDs of all KdpFABC structures obtained in this study. **A** Superimposition of all KdpFABC structures obtained in this study on KdpA, showing few significant deviations in the TMD or KdpC. All E1 conformations shaded in light gray, all E2 conformations in dark gray. **B** Superimposition of all potential potassium ions in the intersubunit tunnel found in all structures presented in this paper. Ions for each structure are presented in a different pink shade.

Table 1 – Table Supplement 1: Cryo-EM data collection, refinement, and validation statistics

	KdpFABC E1·ATP_{early} EMD-14913 [7ZRG]	KdpFABC E1-P·ADP EMD-14917 [7ZRK]	KdpFABC E1-P tight EMD-14912 [7ZRE]	KdpFABC E1-P tight (VO_4^{3-}) EMD-14911 [7ZRD]	KdpFABC E2-P (VO_4^{3-}) EMD-14347	$KdpFAB_{S162A}C$ E1-P·ADP EMD-14919 [7ZRM]	$KdpFAB_{S162A}C$ E2-P EMD-14918 [7ZRL]	$KdpFAB_{D307N}C$ E1 apo tight EMD-14914 [7ZRH]	$KdpFAB_{D307N}C$ E1 apo open 1 EMD-14915 [7ZRI]	$KdpFAB_{D307N}C$ E1 apo open 2 EMD-14916 [7ZRJ]
Data collection and processing										
Magnification	49,407	49,407	49,407	49,407	49,407	49,407	49,407	49,407	49,407	49,407
Voltage (keV)	200	200	200	200	200	200	200	200	200	200
Electron exposure ($e^-/Å^2$)	52	52	52	52	52	52	52	52	52	52
Defocus range (μm)	-0.5 to -2.0	-0.5 to -2.0	-0.5 to -2.0	-0.5 to -2.0	-0.5 to -2.0	-0.5 to -2.0	-0.5 to -2.0	-0.5 to -2.0	-0.5 to -2.0	-0.5 to -2.0
Pixel size (Å)	1.012	1.012	1.012	1.012	1.012	1.012	1.012	1.012	1.012	1.012
Symmetry imposed	C1	C1	C1	C1	C1	C1	C1	C1	C1	C1
Initial particle images (no.)	1,128,433	1,128,433	1,128,433	164,891	164,891	287,232	287,232	728,674	728,674	728,674
Final particle images (no.)	76,121	257,675	114488	74,927	13,508	58,243	46,904	88,852	75,711	47,981
Map resolution (Å)	3.5	3.1	3.4	3.3	7.4	3.7	4.0	3.4	3.5	3.7
FSC threshold	0.143	0.143	0.143	0.143	0.143	0.143	0.143	0.143	0.143	0.143
Map resolution range (Å)	3.3-6.5	3.0-5.5	3.1-5.0	3.1-5.0	N/A	3.5-6.5	3.8-7.0	3.3-5.5	3.4-6.5	3.6-6.5
Refinement										
Initial model used (PDB code)	7NNL	7NNL	6HRA	6HRA	N/A	7NNL	6HRB	6HRA	6HRA	6HRA
Model resolution (Å)	3.7	3.6	3.6	3.5	N/A	4.0	4.1	3.5	3.6	3.7
FSC threshold	0.5	0.5	0.5	0.5	N/A	0.5	0.5	0.5	0.5	0.5
Model resolution range (Å)	80-3.5	80-3.1	80-3.4	80-3.3	N/A	80-3.7	80-4.0	80-3.4	80-3.5	80-3.7
Sharpening B-factor ($Å^2$)	-132	-122	-134	-55	-195	-123	-160	-113	-117	-119
Model composition										
Non-hydrogen atoms	11097	11103	11071	11072	N/A	10890	10782	11065	11065	11065
Protein residues	1456	1456	1456	1456	N/A	1456	1456	1456	1456	1456
Ligands	K: 7 CDL: 2 ATP: 1	K: 13 CDL: 2 ADP: 1 MG: 1	K: 9 CDL: 2	K: 9 CDL: 2 VO4: 1	N/A	K: 5 ADP: 1 MG: 1	K: 1	K: 7 CDL: 2	K: 7 CDL: 2	K: 7 CDL: 2
B factors ($Å^2$)										
Protein	55.0	54.3	50.2	23.8	N/A	54.8	69.9	33.0	52.5	47.5
Ligand	54.8	55.6	40.1	25.9	N/A	116.6	64.4	29.6	49.5	37.8
R.m.s. deviations										
Bond lengths (Å)	0.006	0.006	0.007	0.006	N/A	0.004	0.005	0.004	0.004	0.005
Bond angles (°)	0.849	0.877	0.976	0.893	N/A	0.838	0.908	0.828	0.820	0.908
Validation										
MolProbity Score	1.74	1.72	1.70	1.53	N/A	1.68	1.77	1.73	1.68	1.80
Clash score	7.24	8.04	7.79	5.88	N/A	6.82	8.17	7.43	6.90	9.34
Poor rotamers, %	0.00	0.00	0.00	0.00	N/A	0.00	0.00	0.00	0.00	0.00
Ramachandran plot										
Favored (%)	95.02	95.91	95.98	96.68	N/A	95.64	95.26	94.43	95.71	95.64
Allowed (%)	4.98	4.09	4.02	3.32	N/A	4.36	4.74	4.57	4.29	4.36
Outliers (%)	0.00	0.00	0.00	0.00	N/A	0..00	0.00	0.00	0.00	0.00

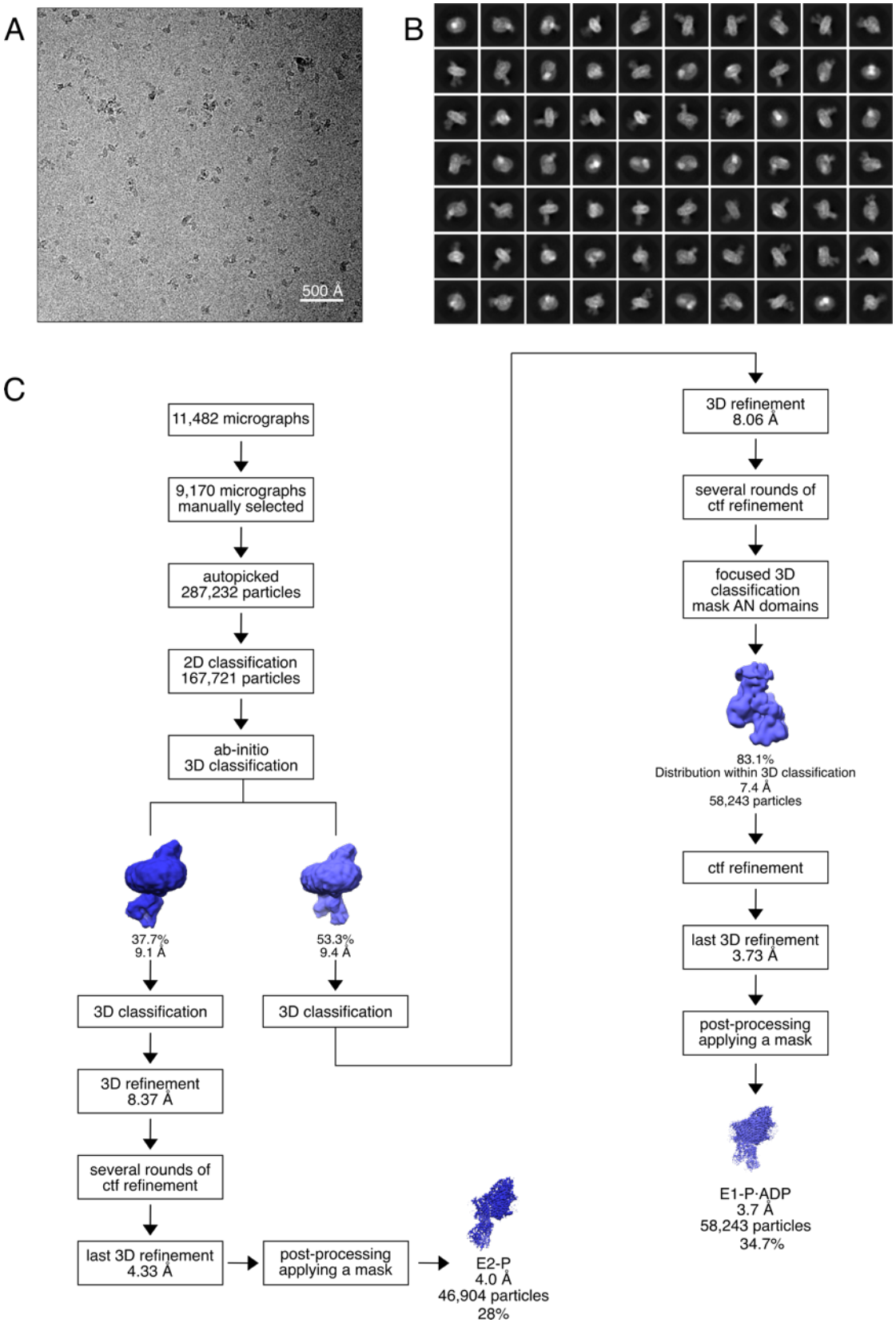

Figure 1 – Figure Supplement 1: Cryo-EM analysis of the KdpFAB$_{S162A}$C complex under turnover conditions, resulting in E1-P·ADP and E2-P states. A Representative cryo-EM image of the recorded data and **B** 2D class averages of vitrified WT KdpFAB$_{S162-P}$C in the presence of 2 mM ATP and 50 mM KCl. **C** Image processing workflow as described in the material and methods. If not otherwise noted, indicated class percentages refer to the initial set of particles defined after 2D classification.

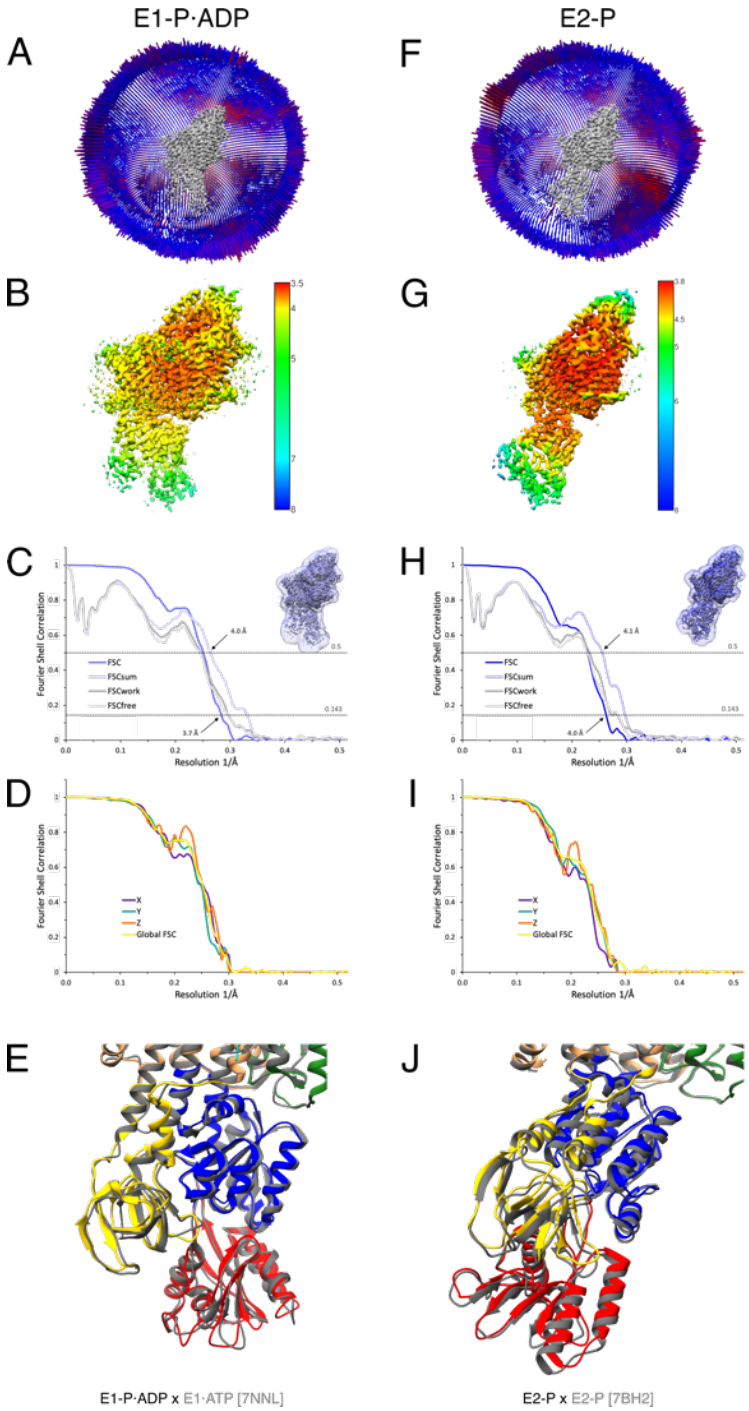

Figure 1 – Figure Supplement 2: Cryo-EM validation of KdpFAB$_{S162A}$C under turnover conditions. Validation shown for the E1-P·ADP (**A-E**) and the E2-P state (**F-J**). **A**,**F** Angular distribution plots of particles included in the final unsymmetrized 3D reconstruction. The number of particles with the respective orientations is represented by length and color of the cylinders (long and red: high number of particles; short and blue: low number of particles). **B**,**G** Final reconstruction maps colored by local resolution as estimated by RELION. **C**,**H** FSC plots used for resolution estimation and model validation. The gold-standard FSC plot between two separately refined half-maps is shown in dark blue and indicates final resolutions of 3.7 Å and 4.0 Å for the E1-P·ADP state (**C**) and the E2-P state (**H**), respectively. The FSC model validation curves for FSCsum, FSCwork and FSCfree are described in material and methods and show no overfitting. Thumbnails of the mask used for FSC calculation overlaid on the maps are shown in the upper right corner of both curves. Dashed lines indicate the FSC thresholds used for FSC (0.143) and for FSCsum (0.5). **D**,**I** Anisotropy estimation plots of the final maps show no significant anisotropy. **E**,**J** Superposition of the E1-P·ADP conformation (colored) with the AMPPCP-stabilized E1·ATP structure [7NNL] (gray), and the E2-P conformation (colored) with the BeF_3^--stabilized E2-P structure [7BH2] (gray), respectively, verifying the assignment of each structure at its position in the conformational cycle.

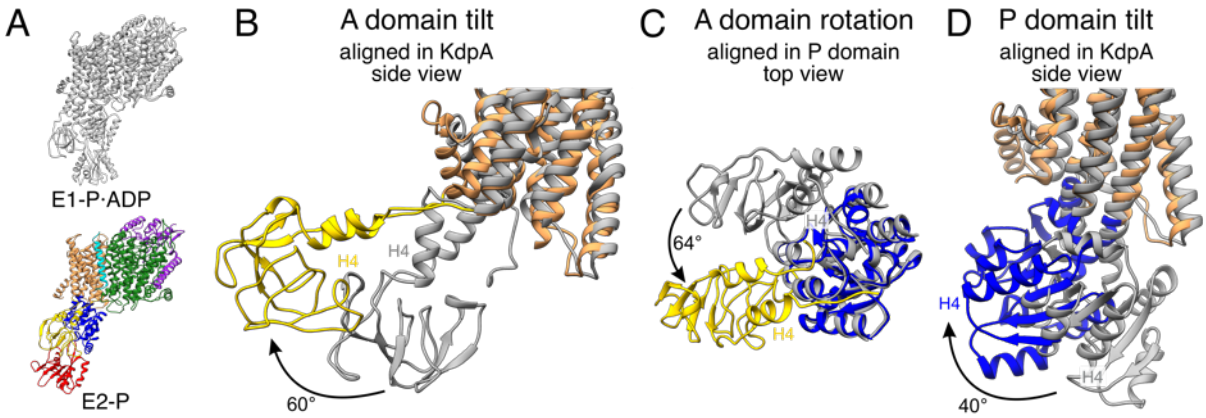

Figure 1 – Figure Supplement 3: A and P domain movements during the E1-P/E2-P transition. **A** KdpFAB$_{S162A}$C structures in the E1-P·ADP (colors) and E2-P (gray) states. Individual panels show (**B**) the tilt of the A domain (structures aligned on the static KdpA, N and P domain removed for clarity), (**C**) the rotation of the A domain around the P domain (structures aligned on the P domain, N domain and the TMD removed for clarity), and (**D**) the tilt of the P domain (structures aligned on the static KdpA, A and N domain removed for clarity). In the E1-P/E2-P transition, the A domain tilts by 60°, while the P domain tilts by 40°. Additionally, the A domain rotates by 64° around the P domain. Helices from the A and P domains used for angle measurements are labelled in all panels.

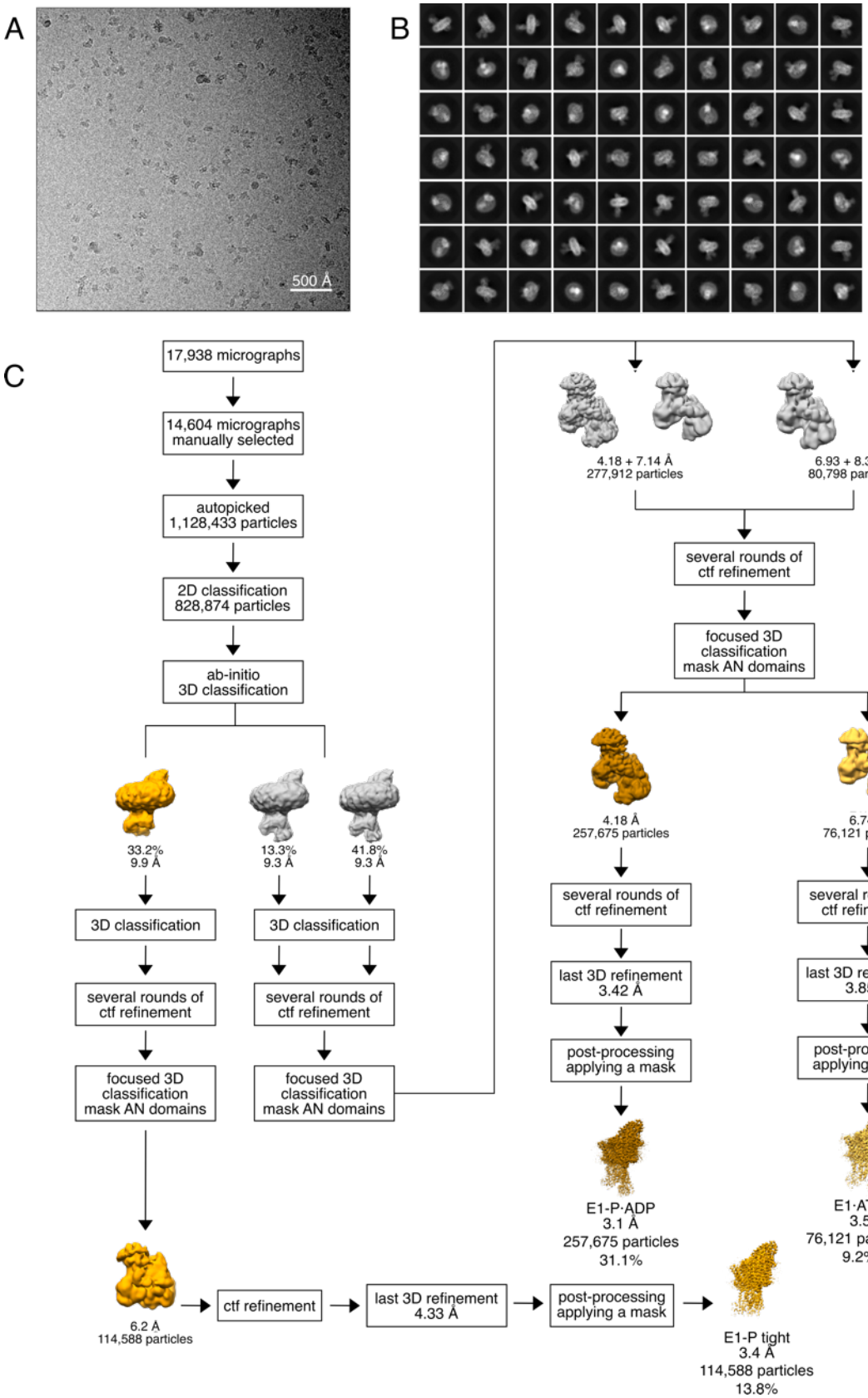

Figure 2 – Figure Supplement 1: Cryo-EM analysis of the WT KdpFAB$_{S162\text{-}P}$C complex under turnover conditions, resulting in the E1-P tight, E1-P·ADP and E1·ATP$_{early}$ states. A Representative cryo-EM image of the recorded data and **B** 2D class averages of vitrified WT KdpFAB$_{S162\text{-}P}$C in the presence of 2 mM ATP and 50 mM KCl. **C** Image processing workflow as described in the material and methods. Indicated class percentages refer to the initial set of particles defined after 2D classification.

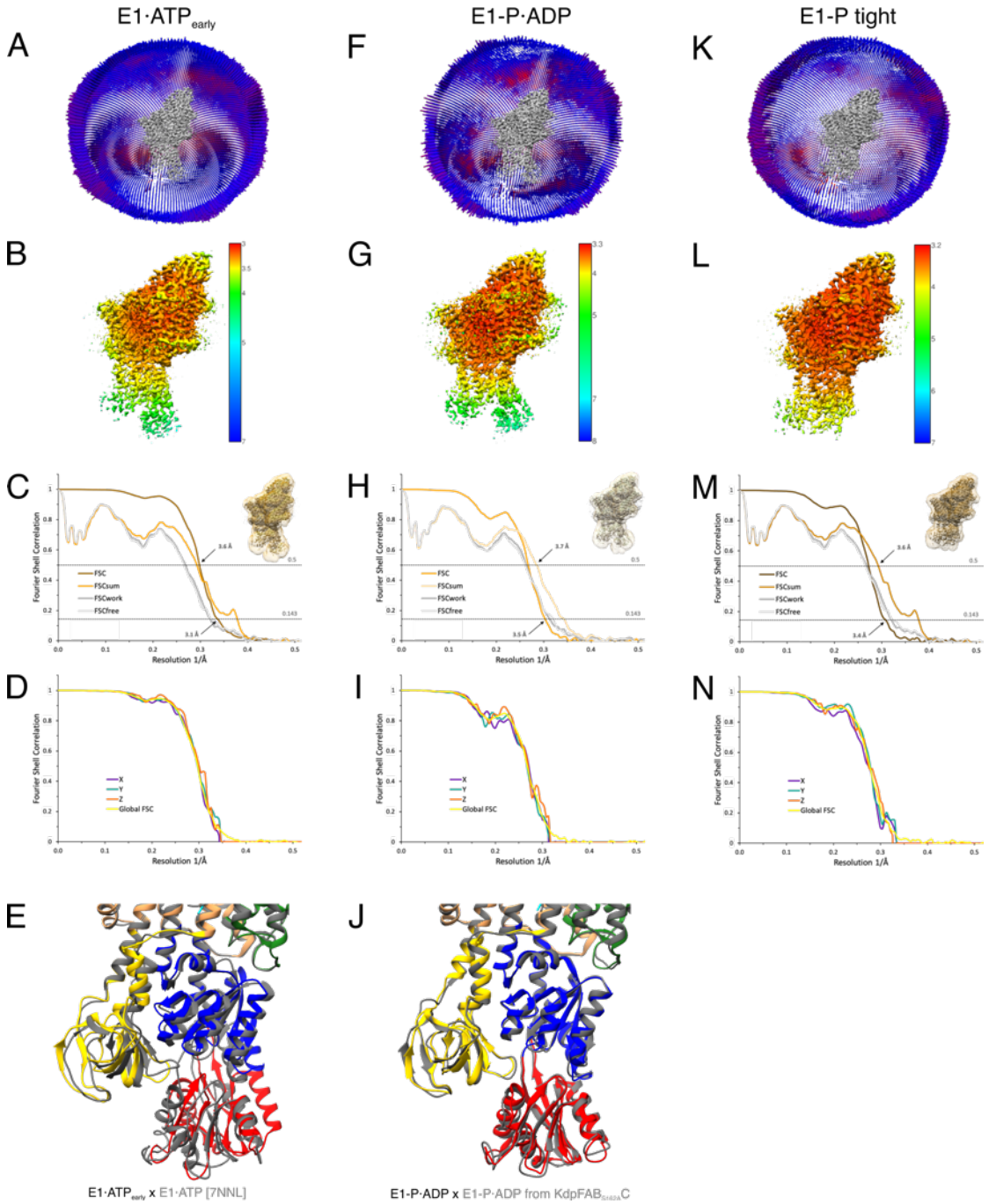

Figure 2 – Figure Supplement 2: Cryo-EM validation of WT KdpFAB$_{S162\text{-}P}$C under turnover. Validation shown for the E1·ATP$_{early}$ state (**A-E**), the E1-P·ADP state (**F-J**), and the E1-P tight state (**K-N**). **A**,**F**,**K** Angular distribution plots of particles included in the final unsymmetrized 3D reconstruction. The number of particles with the respective orientations is represented by length and color of the cylinders (long and red: high number of particles; short and blue: low number of particles). **B**,**G**,**L** Final reconstruction maps colored by local resolution as estimated by RELION. **C**,**H**,**M** FSC plots used for resolution estimation and model validation. The gold-standard FSC plot between two separately refined half-maps indicates final resolutions of 3.5 Å for the E1·ATP$_{early}$ state (C), 3.1 Å for the E1-P·ADP state (**H**) and 3.4 Å for the E1-P tight state (**M**). The FSC model validation curves for FSCsum, FSCwork and FSCfree are described in material and methods and show no overfitting. Thumbnails of the masks used for FSC calculation overlaid on the maps are shown in the upper right corner of the curves. Dashed lines indicate the FSC thresholds used for FSC (0.143) and for FSCsum (0.5). **D**,**I**,**N** Anisotropy estimation plots of the final maps show no significant anisotropy. **E** Superposition of the E1·ATP$_{early}$ structure (colored) with the AMPPCP-stabilized E1·ATP structure [7NNL] (gray), showing a slightly more open N domain in the structure obtained under turnover conditions. **J** Superposition of the E1-P·ADP structure (colored) with the same conformation obtained from KdpFAB$_{S162A}$C under turnover conditions (gray), showing the conformational identity.

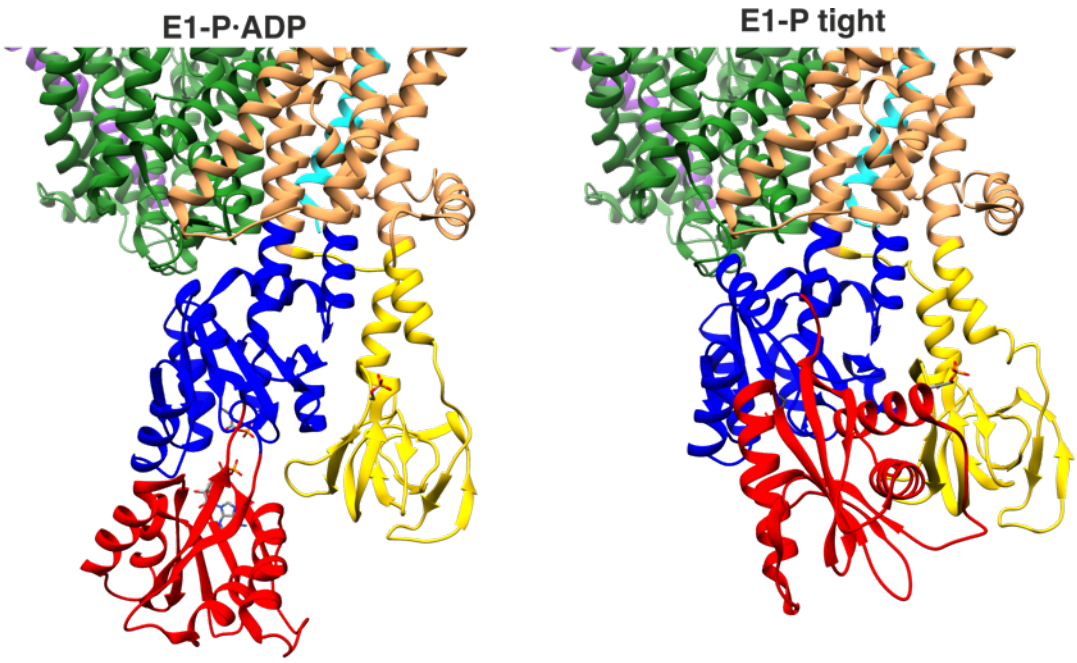

Figure 2 – Figure Supplement 3: Proximity of A and N domains in E1-P·ADP and E1-P tight KdpFABC. In the E1-P tight state, the interface of the N and A domains is significantly increased compared to the low proximity observed in the E1-P·ADP state.

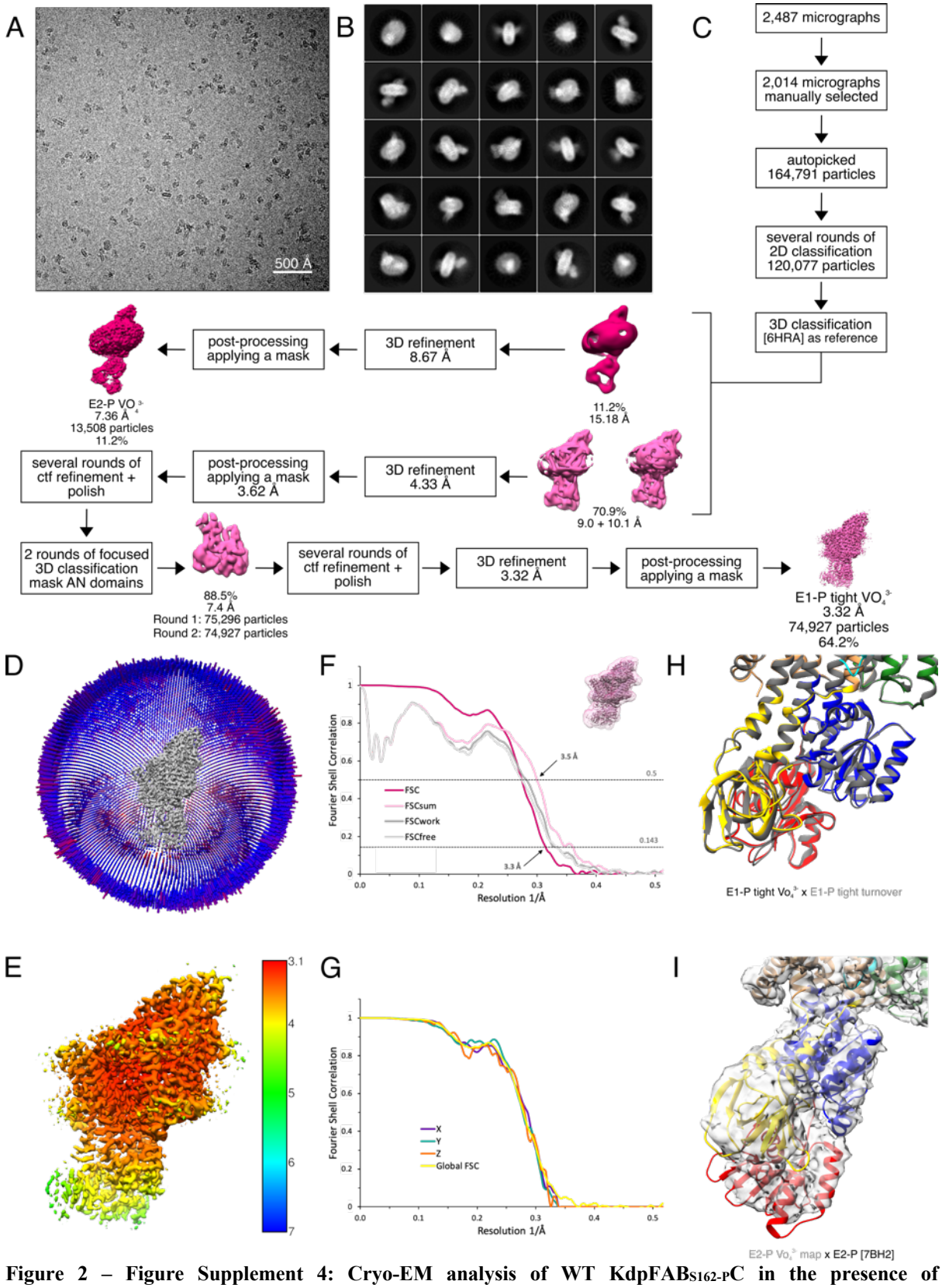

Figure 2 – Figure Supplement 4: Cryo-EM analysis of WT KdpFAB$_{S162\text{-}P}$C in the presence of orthovanadate, resulting in the E1-P tight and E2-P state. A Representative cryo-EM image of the recorded data. **B** 2D class averages of vitrified WT KdpFAB$_{S162\text{-}P}$C in the presence of orthovanadate. **C** Image processing workflow as described in the material and methods section. Indicated class percentages refer to the initial set of particles defined after 2D classification. **D** Angular distribution plot of particles included in the unsymmetrized 3D reconstruction for KdpFABC. The number of particles with the respective orientation is represented by length and color of the cylinders (long and red: high number of particles; short and blue: low number of particles). **E**

Final reconstruction map of the E1-P tight state colored by local resolution as estimated by RELION. **F** FSC plot used for resolution estimation and model validation of the E1-P tight state. The gold-standard FSC plot between two separately refined half-maps is shown in red and indicates a final resolution of 3.3 Å. The FSC model validation curves for FSCsum, FSCwork and FSCfree are described in the methods and show no overfitting. A thumbnail of the mask used for FSC calculation overlaid on the map is shown in the upper right corner. Dashed lines indicate the FSC thresholds used for FSC (0.143) and for FSCsum (0.5). **G** Anisotropy estimation plot of the final E1-P tight map, showing no significant anisotropy. **H** Superposition of the E1-P tight structure obtained in the presence of orthovanadate (colored) with the E1-P tight structure of $KdpFAB_{S162\text{-}P}C$ obtained under turnover conditions (gray), showing that the adopted conformation is identical. **I** Fit of the BeF_3^--stabilized E2-P structure [7BH2] (colored) into the E2-P map obtained in the presence of orthovanadate (gray), verifying the assignment of the E2-P conformation.

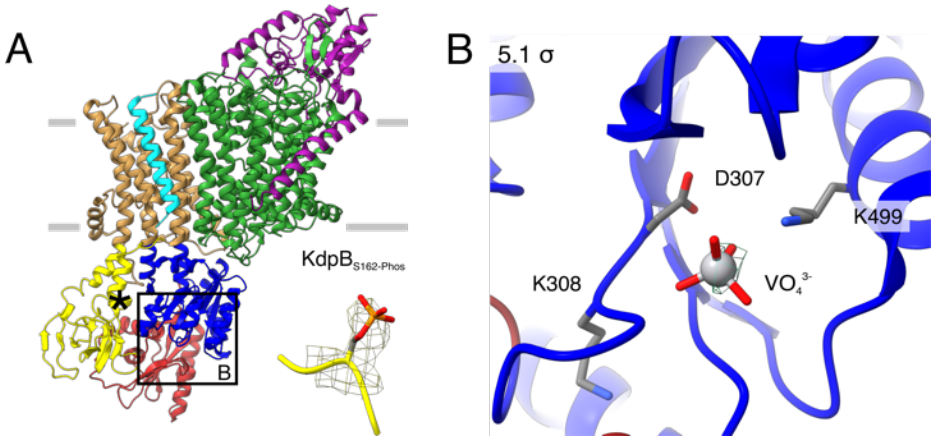

Figure 2 – Figure Supplement 5: E1-P tight structure of WT KdpFAB$_{S162\text{-}P}$C in the presence of orthovanadate. A The E1-P tight structure obtained from KdpFAB$_{S162\text{-}P}$C in the presence of orthovanadate with the KdpB$_{S162}$ phosphorylation highlighted. **C** Nucleotide binding site in the P domain of the E1-P tight conformation, showing the coordinated orthovanadate (VO_4^{3-}) that mimics phosphorylation of the catalytic KdpB$_{D307}$. Densities are shown at the indicated σ level.

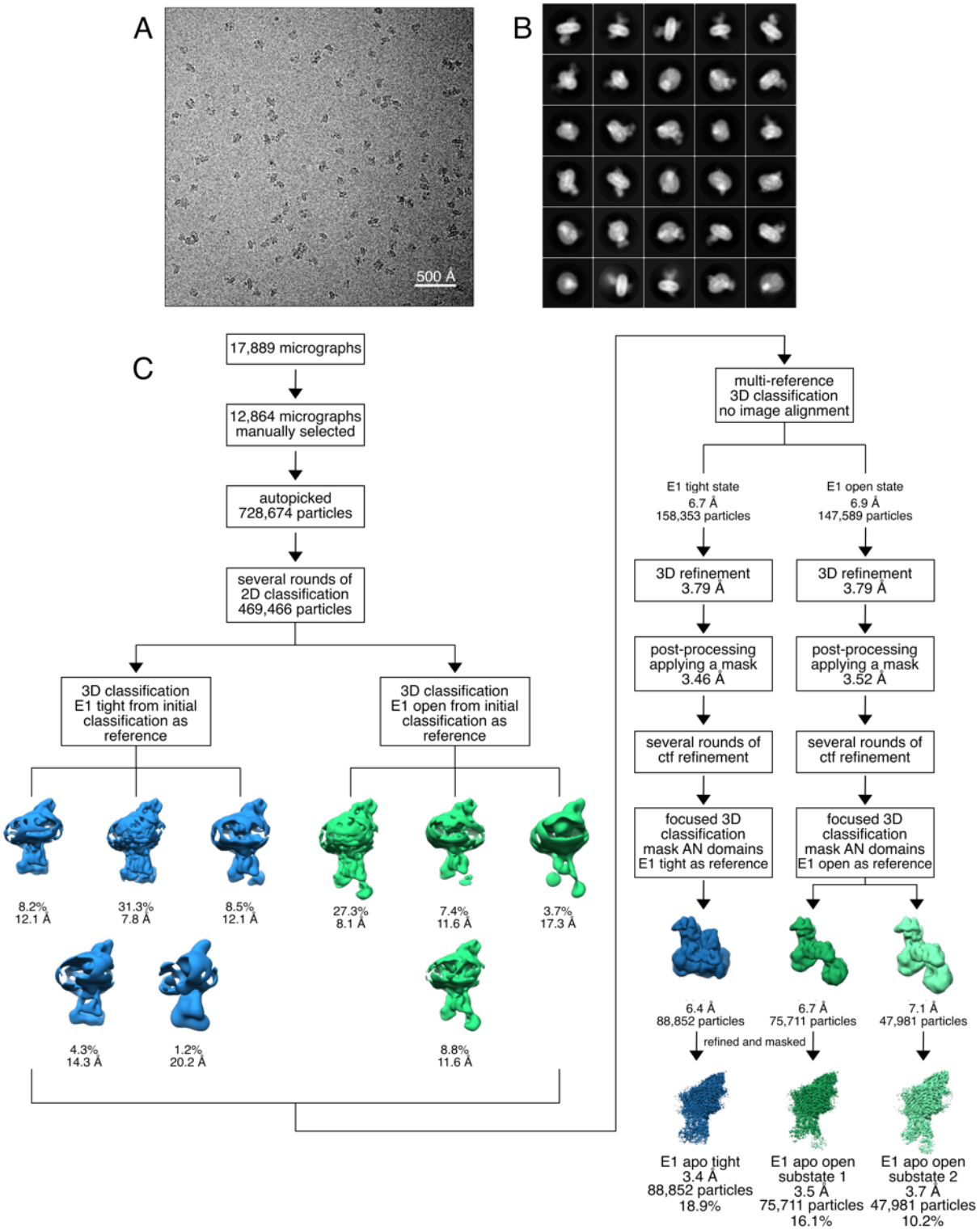

Figure 3 – Figure Supplement 1: Cryo-EM analysis of the KdpFAB$_{S162\text{-}P/D307N}$C complex in the absence of nucleotide, resulting in the E1 apo tight and E1 apo open states. A Representative cryo-EM image of the recorded data. **B** 2D class averages of vitrified KdpFAB$_{S162\text{-}P/D307N}$C in the presence of 50 mM KCl. **C** Image processing workflow as described in the material and methods. Indicated class percentages refer to the initial set of particles defined after 2D classification.

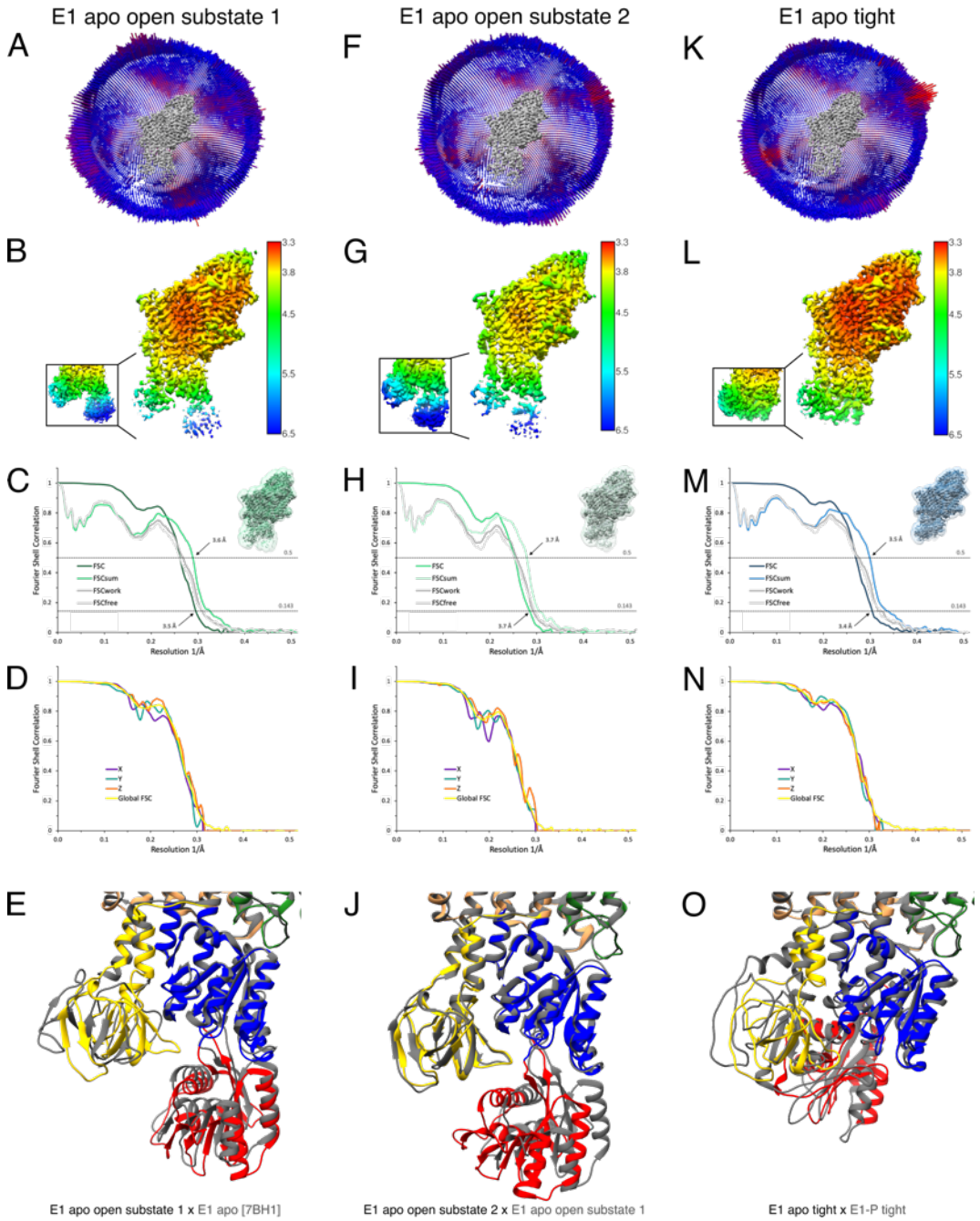

Figure 3 – Figure Supplement 2: Cryo-EM validation of WT KdpFAB$_{S162-P/D307N}$C under nucleotide-free conditions. Validation shown for E1 apo open substate 1 (**A-E**), E1 apo open substate 2 (**F-J**) and the E1 apo tight state (**K-O**). **A**,**F**,**K** Angular distribution plot of particles included in the final unsymmetrized 3D reconstruction. The number of particles with the respective orientations is represented by length and color of the cylinders (long and red: high number of particles; short and blue: low number of particles). **B**,**G**,**L** Final reconstruction maps colored by local resolution as estimated by RELION. Inset shows N, P, and A domains at higher contour level. **C**,**H**,**M** FSC plots used for resolution estimation and model validation. The gold-standard FSC plot between two separately refined half-maps indicates final resolutions of 3.5 Å for the E1 apo open substate 1 (**C**), 3.7 Å for the E1 apo open substate 2 (**H**), and 3.4 Å for the E1 apo tight state (**M**). The FSC model validation curves for FSCsum, FSCwork and FSCfree are described in material and methods and show no overfitting. Thumbnails of the masks used for FSC calculation overlaid on the map are shown in the upper right corner of the curves. Dashed lines indicate the FSC thresholds used for FSC (0.143) and for FSCsum (0.5). **D**,**I**,**N** Anisotropy estimation plots of the final maps show no significant anisotropy. **E** Superposition of E1 apo open substate 1 (colored) with the E1 apo structure [7BH1] (gray), verifying the conformational assignment. **J** Superposition of the E1 apo open substate 2 (colored) with E1 apo open substate 1 (gray), showing a slightly different arrangement of the N domain. **O** Superposition of the E1 apo tight state with the E1-P tight state obtained under turnover conditions, showing a different arrangement of the cytosolic domains.

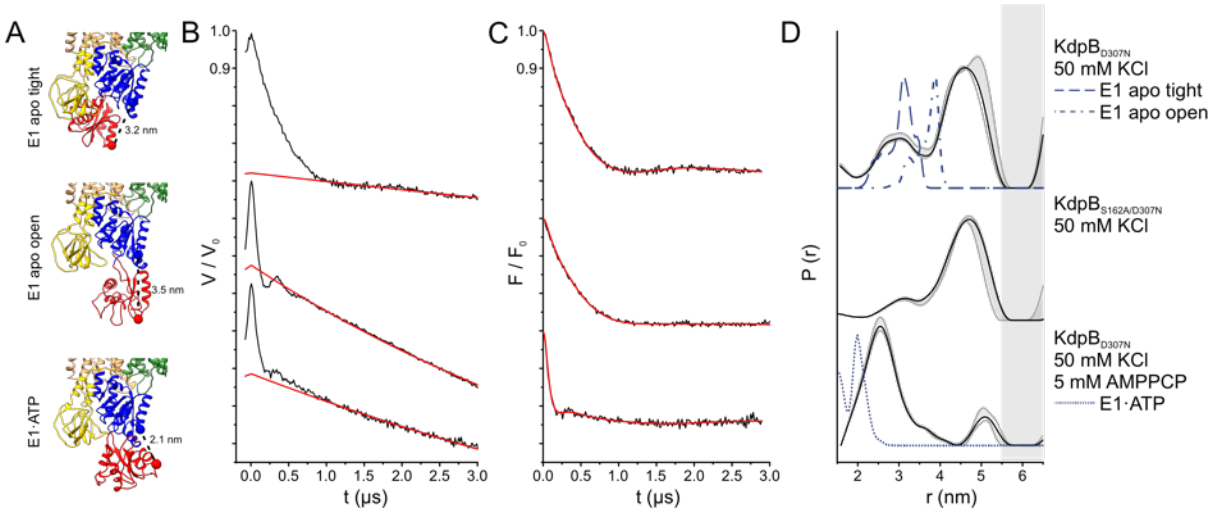

Figure 4 – Figure Supplement 1: Pulsed EPR measurements of KdpFABC variants in the absence and presence of AMPPCP. A Cytoplasmic domains of the anticipated states with expected C_α-C_α distances indicated. **B** Experimental raw data V(t) with fitted background function (red). **C** Background-corrected dipolar evolution function F(t) with applied fit (red). **D** Interspin distance distribution P(r) (black curves) obtained by Tikhonov regularization. Gray background curves indicate the full variation of possible distance distributions. The lower and upper error estimates (blue lines) represent the respective mean value minus and plus two times its standard deviation, respectively; the larger the deviations, the less reliable the predicted distances. Dashed gray lines represent the predicted distance distributions of the E1 apo tight, the E1 apo open and the E1·ATP states, respectively, using the MMM rotamer library analysis. Gray shaded areas starting at 5.5 nm indicate unreliable distances.

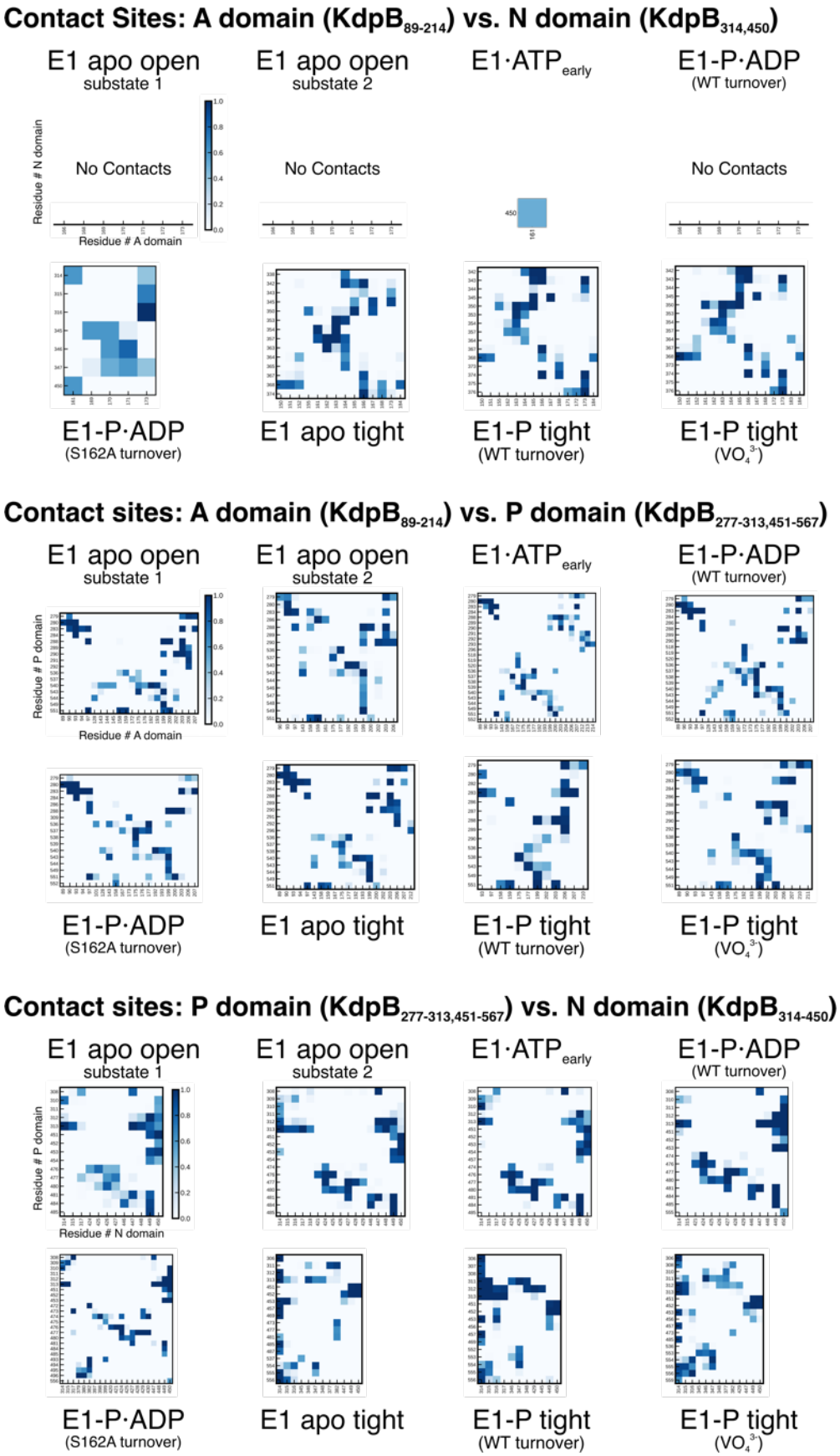

Figure 4 – Figure Supplement 2: KdpB$_{S162-P}$ mediates stabilization of the E1-P tight state. A Contact site analysis of the KdpB N, P and A domains in the E1 conformations of KdpFABC. For each structure, graphs show contact sites observed over 3x50 ns MD simulations, where darker squares represent longer contact in the simulation time. Empty x-axes indicate no contacts.

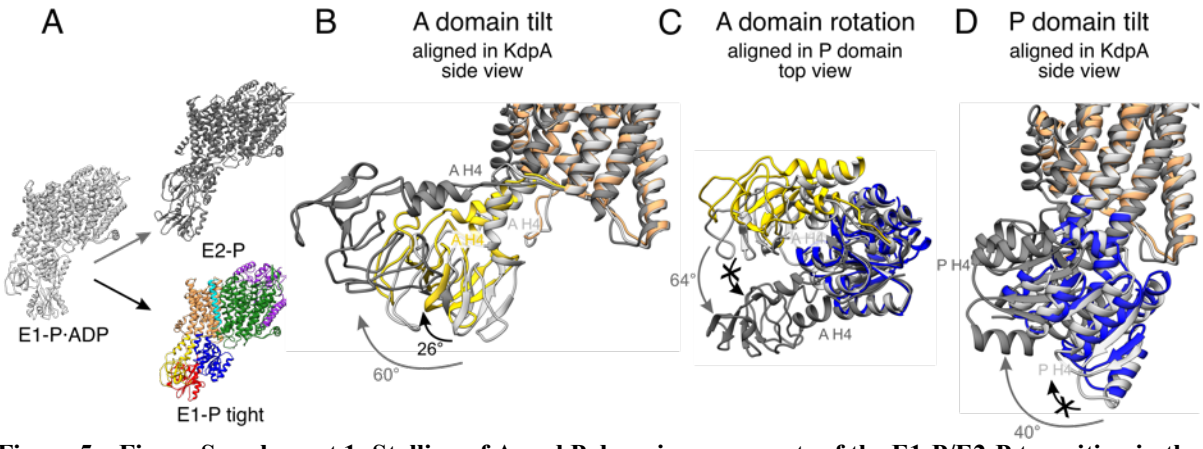

Figure 5 – Figure Supplement 1: Stalling of A and P domain movements of the E1-P/E2-P transition in the E1-P tight state. A Comparison of KdpFAB$_{S162\text{-}P}$C in the E1-P tight state (colored) with KdpFAB$_{S162A}$C in the E1-P·ADP (light gray) and E2-P (dark gray) states. Individual panels show (**B**) the tilt of the A domain (structures aligned on the static KdpA, N and P domain removed for clarity), (**C**) the rotation of the A domain around the P domain (structure of the cytosolic domains aligned on the P domain, N domain and the TMD removed for clarity), and (**D**) the tilt of the P domain (structures aligned on the static KdpA, A and N domain removed for clarity). During the E1-P/E2-P transition (gray arrows), the A domain tilts by 60°, while the P domain tilts by 40°. Additionally, the A domain rotates by 64° around the P domain. The E1-P tight state shows a partial 'attempted' transition (black arrows), with a tilt of the A domain by 26°, although the P domain does not undergo global rearrangements and the A domain does not complete its rotation around the P domain. Helices from the A and P domains used for angle measurements are labelled in all panels.

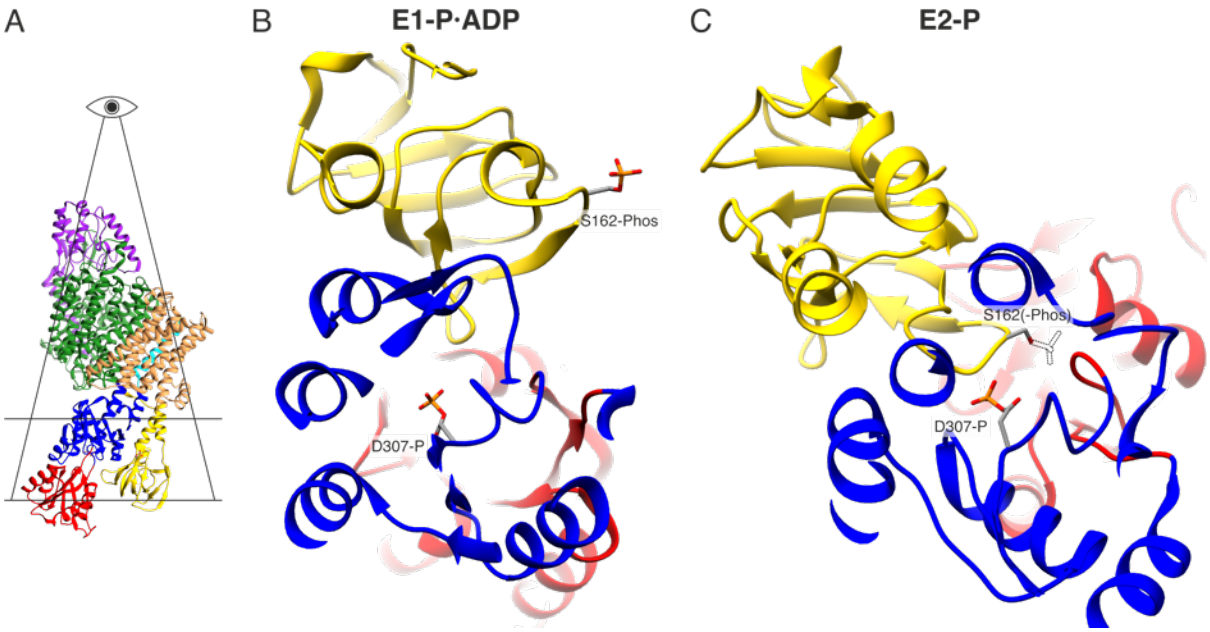

Figure 5 – Figure Supplement 2: Electrostatic repulsion of KdpB$_{S162\text{-}P}$ and KdpB$_{D307\text{-}P}$ during the E1-P/E2-P transition. A Highlighted section displayed in **B**. **B** View of the proximity between KdpB$_{D307\text{-}P}$ and KdpB$_{S162\text{-}P}$ in the E1-P·ADP and hypothetical E2-P states. The transition to the E2-P state is not possible in the inhibited KdpFAB$_{S162\text{-}P}$C, since the catalytic phosphate would come in close proximity with the inhibitory KdpB$_{S162\text{-}P}$, whose theoretical position in the E2-P state is shown as a dashed outline.